3-2023

GENERATING SYNTHETIC SATELLITE IMAGES OF MARS DUST STORMS BASED ON RADIATIVE TRANSFER MODELS, AS A FOLLOW-ON APPLICATION OF MARSWRF DUST CYCLE SIMULATIONS

Fatima Ali Alkaabi

GENERATING SYNTHETIC SATELLITE IMAGES OF MARS DUST STORMS BASED ON RADIATIVE TRANSFER MODELS, AS A FOLLOW-ON APPLICATION OF MARSWRF DUST CYCLE SIMULATIONS

Fatima Ali Abdulla Alkaabi

March 2023

United Arab Emirates University
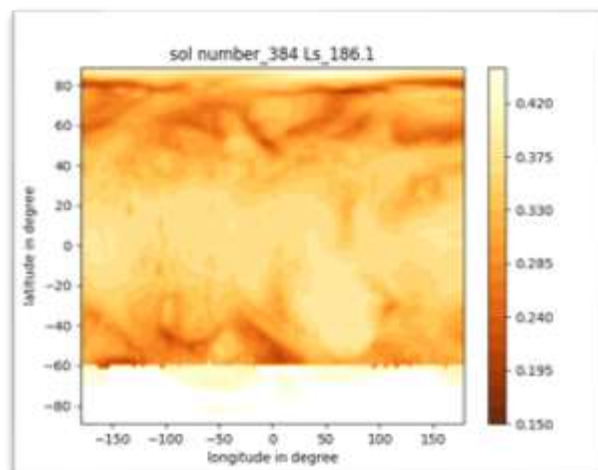
College of Science

Department of Physics

GENERATING SYNTHETIC SATELLITE IMAGES OF MARS
DUST STORMS BASED ON RADIATIVE TRANSFER MODELS,
AS A FOLLOW-ON APPLICATION OF MARSWRF DUST CYCLE
SIMULATIONS

Fatima Ali Abdulla Alkaabi

This thesis is submitted in partial fulfilment of the requirements for the degree Master of
Science in Space Science

March 2023

Cover: Plot of a synthetic satellite image of a regional dust storm (670 nm) in 2° × 2° grid resolution (latitude by longitude) in MY14 of Gebhardt et al.(2020) model years at sol 384 Ls 186°.

(Photo: By Fatima Ali Abdulla Alkaabi)

Declaration of Original Work

I, Fatima Ali Abdulla Alkaabi, the undersigned, a graduate student at the United Arab Emirates University (UAEU), and the author of this thesis entitled "*Generating Synthetic Satellite Images of Mars Dust Storms Based on Radiative Transfer Models, as a Follow-on Application of MarsWRF Dust Cycle Simulations*", hereby, solemnly declare that this is the original research work done by me under the supervision of Dr. Abdelgadir Abuelgasim, in the College of Science at UAEU. This work has not previously formed the basis for the award of any academic degree, diploma or a similar title at this or any other university. Any materials borrowed from other sources (whether published or unpublished) and relied upon or included in my thesis have been properly cited and acknowledged in accordance with appropriate academic conventions. I further declare that there is no potential conflict of interest with respect to the research, data collection, authorship, presentation and/or publication of this thesis.

Student's Signature: _____

Date: ___20 March 2023___

Advisory Committee

1) Advisor: Dr Abdelgadir Abuelgasim

Title: Associate Professor

Department of Geography and Urban Sustainability

College of Humanities & Social Science

2) Co-advisor: Dr. Claus Gebhardt

Title: Assistant Professor

Department of Physics

College of Science

Approval of the Master Thesis

This Master Thesis is approved by the following Examining Committee Members:

1) Advisor (Committee Chair): Dr Abdelgadir Abuelgasim
   Title: Associate Professor
   Department of Geography and Urban Sustainability
   College of Humanities & Social Science

   Signature _____   Date __10 May 2023__

2) Member: Dr Roland Young
   Title: Assistant Professor
   Department of Physics
   College of Science
   Signature _____   Date __17 May 2023__

3) Member (External Examiner): Dr Javier Martin-Torres
   Title: Chair Professor of Planetary Sciences
   Department of Geosciences
   Institution: University of Aberdeen, UK

   Signature _____   Date __18 May 2023__

This Master Thesis is accepted by:

Dean of the College of Science: Professor Maamar Benkraouda

Signature *Maamar Benkraouda*

Date June 5, 2023

Dean of the College of Graduate Studies: Professor Ali Al-Marzouqi

Signature Ali Hassan

Date June 6, 2023

Abstract

Dust is a fundamental component of the Martian atmosphere; it plays a vital role in the planet's climate system and atmospheric variability. For these reasons, it is considered one of the essential keys to understanding the Martian atmosphere's behavior. The dust events on Mars range from local/regional dust storms that occur every Martian year to global dust storms that have only been observed, on average, once every 3-4 Martian years. The large regional and global dust storms have strong thermal and dynamic effects on the atmosphere. MarsWRF is a Mars version of the terrestrial numerical weather and climate model WRF (Weather Research and Forecasting Model) and part of the PlanetWRF models for planetary atmosphere research. This project aims to convert MarsWRF output data into synthetic satellite images of Mars dust storms of different sizes by using the radiative transfer model DISORT. The imagery is generated by passing selected variables from the MarsWRF output through the DISORT model, which is used to compute the top-of-the-atmosphere reflectance for a given band. The main results are synthetic satellite images plotted in 670 nm with a grid resolution of 2° × 2° of different dust events during one year of the MarsWRF model run. The obtained results of this project are consistent with the real cases of satellite images of Mars dust storms.

Keywords: Dust, Atmosphere, Storms, Mars, Images, MarsWRF, Synthetic Satellite Images.

Title and Abstract (in Arabic)

إنتاج صور ستالايت صناعية لعواصف المريخ الترابية بناءً على نمذجة النقل الإشعاعي، كتطبيق متابعة لمحاكاة دورة الغبار MarsWRF

الملخص

يُعتبر الغبار عنصراً أساسيّاً في تكوين الغلاف الجوّي لكوكب المريخ، حيث يلعبُ دوراً مهمّاً في النظام المناخي للكوكب وتقلّباته الجويّة، لذلك يُعتبر أحد المفاتيح المهمّة لفهم سلوك الغلاف الجوي للمرّيخ. تتنوع أحداث الغبار على المريخ وتتراوح ما بين (محلي / إقليمي) والذي يحدث كل سنة مريخيه، إلى عواصف ترابيه عالميه تحدث بمعدل كل ثلاث إلى أربع سنواتٍ مريخية. العواصف الترابية الاقليمية الكبيرة والعالمية تؤثر حرارياً وديناميكياً على الغلاف الجوي. هذا المشروع يهدف الى تحويل البيانات المخرجة من MarsWRF الى صور ساتلايت اصطناعية لعواصف المريخ الترابية في نطاقات مختلفة باستخدام نموذج النقل الاشعاعي . DISORT Mars WRF هو نظام مشابه للنظام المناخي الرقمي لكوكب الأرض, ولكن بنسخة خاصة لكوكب المريخ (نموذج أبحاث الطقس والتنبؤات الجوية) وهو جزء من نموذج الابحاث الجوية للكواكب PlanetWRF. يتم انشاء هذه الصور بواسطة تمرير متغيرات محددة من مخرجات MarsWRF من خلال نموذج DISORT، وهذا يستخدم لحساب انعكاس الجزء العلوي من الغلاف الجوي لنطاق معيّن. النتائج الرئيسية هي صور أقمار صناعية اصطناعية مرسومة يتم رسمها في الطول الموجي 670 نانومتر مع شبكة بوضوح $2°\times 2°$ لأحداث عواصف ترابية مختلفة خلال سنة واحدة من تشغيل نموذج Mars WRF. النتائج التي حصلنا عليها من هذا المشروع متوافقة مع الحالة الحقيقية لصور الأقمار الصناعية المُلتقطة للعواصف الترابية على كوكب المريخ.

مفاهيم البحث الرئيسية: غبار، غلاف جوي، عواصف، المريخ، صور، MarsWRF، صور ستالايت اصطناعيه.

Acknowledgements

Dedication

To my beloved father

Ali Abdulla Alkaabi
I pray that his soul rest in peace

Table of Contents

List of Tables

List of Figures

List of Abbreviations

ACS	Atmospheric Chemistry Suite
AER	Atmospheric & Environmental Research
CDOD	Column Dust Optical Depth
DISORT	Discrete-Ordinate-Method Radiative Transfer
DPI	Derived Product Imagery
EDL	Entry, Descent, and Landing
EMIRS	Emirates Mars Infrared Spectrometer
EMM	Emirates Mars Mission
ESRL	Earth System Research Laboratory
EXI	Emirates eXploration Imager
GCM	General Circulation Model
GOES	Geostationary Operational Environmental Satellite
LS	Solar Longitude
MARCI	Mars Color Imager
Mars PCM	Mars Planetary Climate Model
MarsWRF	Mars Weather Research And Forecasting Model
MCS	Mars Climate Sounder
MGCMs	Mars Global Climate Models
MGS	Mars Global Surveyor
MOC	Mars Observer Camera
MOLA	Mars Orbiter Laser Altimeter
MRO	Mars Reconnaissance Orbiter
MY	Martian Year
N-HB	Northern Hellas Basin

N-OM	North of Olympus Mons
NASA	National Aeronautics and Space Administration
NCAR	National Center For Atmospheric Research
NetCDF	Network Common Data Form
NOAA	National Oceanic and Atmospheric Administration
NSSL	National Severe Storms Laboratory
NWP	Numerical Weather Prediction
PBL	Planetary Boundary Layer
RTM	Radiative Transfer Model
S-CP	South of Chryse Planitia
S-HB	Southern Hellas Basin
TES	Thermal Emission Spectrometer
TGO	Trace Gas Orbiter
TOA	Top of Atmosphere
WRF	Weather Research and Forecasting Model
WRF-ARW	Advanced Research of the Weather Research and Forecasting

Chapter 1: Introduction

1.1 Overview

Generally, Mars is well-known for its dust storms. Scientists have been tracking the dynamic mechanism of the dust for more than a century. They were able to infer their existence through direct and indirect ways. Indirectly, by the changes in the pressure or temperature in specific regions. Directly from both telescopes on Earth and spacecraft orbiting Mars. Their observations concluded that dust lift occurs on Mars in several forms depending on the event's size. Understanding the Martian atmosphere and dust behavior cannot be entirely done with the available data observation alone. It also required using numerical models, which have developed and improved over the past years. Joining both approaches will lead to a deep knowledge of Mars and its atmosphere. This work aims to convert MarsWRF output data into synthetic satellite images (i.e., artificial satellite images) using a second model. The latter will be given by a radiative transfer model (e.g., DISORT). MarsWRF model is the Mars version of the Weather Research and Forecasting Model (WRF) and is part of the PlanetWRF. It is designed to simulate the Martian atmosphere for many Martian years (MYs). The focus of the generated images is the Mars dust storms in different sizes at different times of the Martian year. This thesis has four chapters. Chapter 1 provides an introduction and summarizes existing literature. Chapter 2 describes the method and process of the work. Chapter 3 presents synthetic satellite images. Chapter 4 is the conclusions part.

1.2 Statement of the Problem

Learning more about the Martian dust and how the storms form and evolve is crucial. The dynamical mechanisms of dust events' onset, expansion, and decay are not fully understood. Numerical models that consider the Martian system's thermal and dynamic conditions can be viewed as an optimal approach to fill the existing gaps and do simulations to provide potential observations of the planet's surface during specific conditions. This project will involve simulating observations using two numerical models (MarsWRF) and the other model the radiative transfer model (DISORT) to produce synthetic satellite images and then compare them with real existing images from satellites. The benefit of this work is the ability to:

1.) Evaluate and refine the model performance

2.) The development and verification of satellite instruments and related data production algorithms and data applications.

On Earth, synthetic satellite imagery has numerous applications in weather forecasting. The capability to apply forecasting on Mars dust storms in advance can give a chance to put specific mitigation approaches. Moreover, we can take advantage of synthetic satellite images regarding upcoming/future Mars satellite missions and their data exploration.

1.3 Research Objectives

This project aims to: 1.) run a radiative transfer model (DISORT) with output data from the MarsWRF model

2.) Generate synthetic satellite images of Mars dust storms and optimize their quality

3.) Provide evidence of how far the integrated perspective of synthetic satellite images adds value to the output data of the MarsWRF model

1.4 Relevant Literature

1.4.1 Dust Cycle

Mars and Earth have partly similar geophysical systems, i.e., cryospheres, lithospheres, and atmospheres. About the latter, both planets have thin atmospheres and are relatively transparent to sunlight, as well as having a similar spin rate and axial tilt (Haberle, 2003), yet there are notable differences between them; the amount of carbon dioxide in the Martian atmosphere represents twice the amount found in the Earth's atmosphere. The Martian atmosphere is composed entirely of carbon dioxide with an average of 95.1% (Haberle et al., 2017), much lower surface pressure on Mars with an average of 6.1 hPa, besides a weak magnetic field along with the absence of a hydrological cycle to release latent heat into the atmosphere (Haberle, 2003). The Martian atmosphere can be divided into three regions: the lower atmosphere (up to 50 km), the middle atmosphere (50-100 km), and the upper atmosphere (above 100 km)

(Almatroushi et al., 2021). The majority of solar interactions take place in the lower part of the atmosphere; the absorption, reflection, or scattering of the incoming solar radiation occurs by dust and gases in the lower atmosphere or the surface, as Figure 1 illustrates (Wolff et al. 2017). Due to the abundant constituent of dust on the Martian surface and the lower-middle atmosphere (Almatroushi et al., 2021), it was considered one of the critical feature drivers of the meteorology and climatology of the Martian atmosphere (Kass et al., 2016).
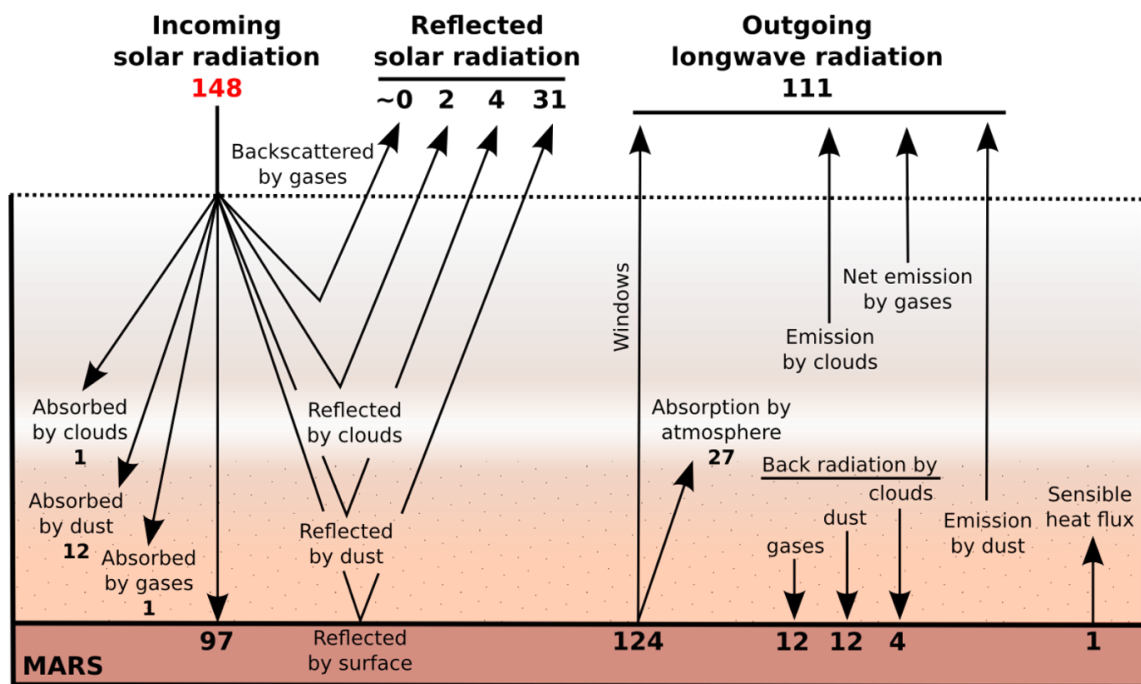
Figure 1: Solar interaction (Wolff et al., 2017)

In order to understand the behavior of the Martian atmosphere, a profound knowledge of the dust cycle is needed (Gebhardt et al., 2020). On Mars, in general, The dust cycle refers to the various processes on the planet that cause dust to move around its atmosphere and surface over time (Newman & Richardson, 2015), starting with the dust lifted from the surface into the atmosphere by strong winds and dust devils and is subsequently transported by atmospheric circulation and deposited back onto the surface (Montabone et al., 2020). The balance between the lifted and sedimented dust can indicate atmospheric dustiness (Newman & Richardson, 2015). Dust moving around the

atmosphere and surface changes the planet's climate by affecting how much energy it absorbs and reflects (Newman & Richardson, 2015) since Martian dust aerosols are radiatively active (Montabone et al., 2020). Consequently, the dust cycle strongly influences atmospheric variability (Montabone et al., 2005), considering it an essential process controlling the Martian atmospheric circulations on a wide range of time scales (Montabone et al., 2020).

Dust storms are one of the defining features of the Martian atmosphere. According to Cantor (2007) and based on MOC observations of different types of dust events ranging from local to regional and global dust storms (see Figure 2), once the dust is lifted into the atmosphere, it may stay suspended there for a certain period ranging from less than a single sol to more than 150 sols in the global dust storms events. Based on observations and modeling, the main reason for generating dust storms is the strong surface dust lifting (Gebhardt et al., 2021), few regions with strong dust lifting act as sources for most of the dust deposited on the planet. Montabone et al. (2005) state that some meteorological variables can significantly drive dust lifting, such as differences in the near-surface wind stress, surface-to-air temperature, and thermodynamic efficiency.
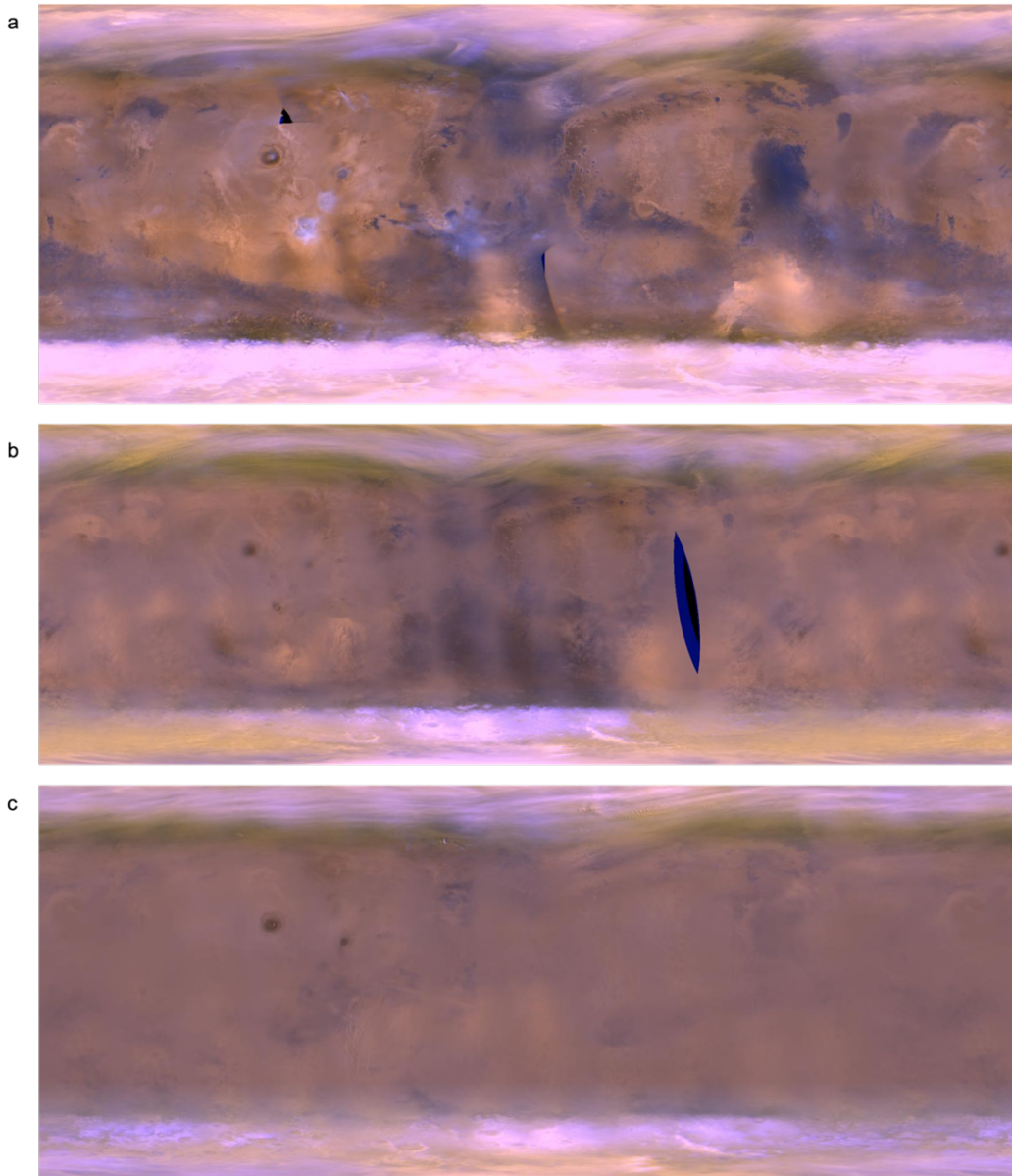
Figure 2: Satellite images of three different dust storms, Local, regional, and global.

(a) Local dust storm near the northeastern border of Hellas Jun 16, 2001 (sol 6) at Ls 179.1° (b) regional dust storm over Syria Jun 5, 2001, at Ls 189.6° (c) global dust storm July 16, 2001 (sol 36) Ls 196° (MOC observations).

Typically, in most portions of the lower atmosphere, there is always a background haze of dust, except for the winter polar vortex (Kass et al., 2016). Even during the clearest atmospheric conditions, there is some interaction between the incoming solar radiation with the suspended aerosols before reaching the surface, resulting in a

significant effect of atmospheric dust on surface observations and images (Christensen, 1988). This suspended dust can be seen in the orbital imaging as a blurring haze (see Figure 3). It is thought that dust devils maintain the background dust haze load of the Martian atmosphere (Basu, 2004). However, the slow sediment of the lifted dust by dust storms is excluded as an explanation for the background haze, as outside the dust storm season, there is still repeatable high dust loading from year to year (Kahanpää et al., 2016). Newman and Richardson (2015) refers to the background dust cycle as the variation of opacity and air temperature in the absence of significant dust events such as regional and global dust storms.
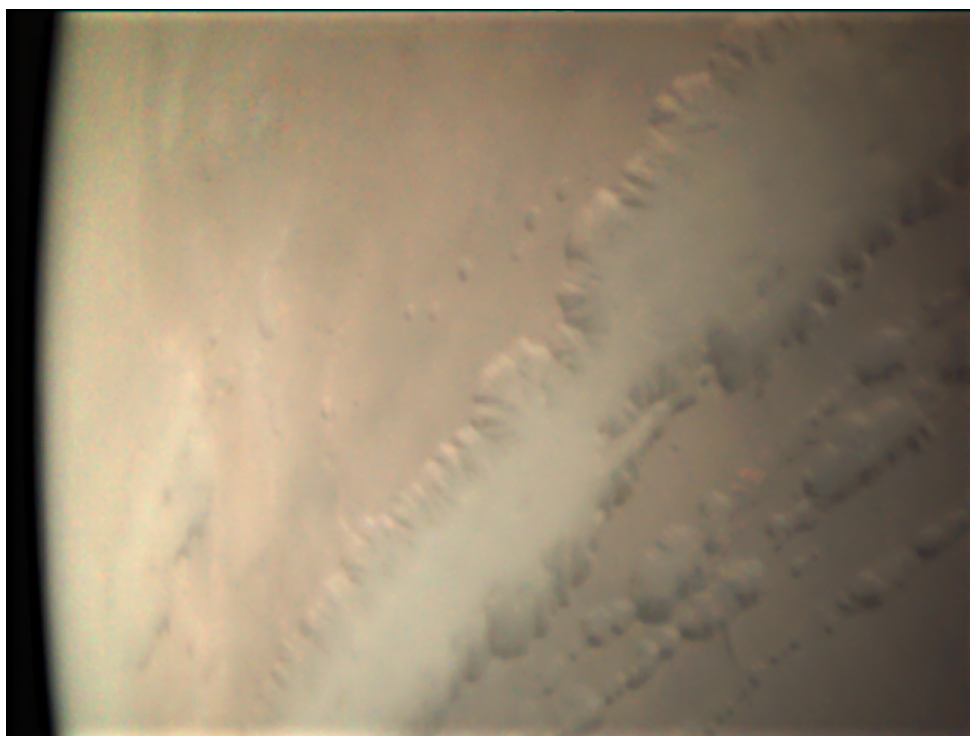
Figure 3: Part of Valles Marineris with hazes present (12 November 2018), image taken by the VMC camera (planetary Science Archive)

1.4.2 Dust Devils

One of the main mechanisms of transporting and lifting dust from the ground into the atmosphere is dust devils. They are a small-range phenomenon of whirlwinds of warm air with winds strong enough to lift dust and commonly happen in arid areas (Hueso et al., 2023). Dust devils are atmospheric convective vortices with a low-pressure core with strong updrafts that lift and entrain particles of all sizes from the surface

(Kahanpää et al., 2016). The dip in the pressure record and the sharp changes in wind intensity and direction can be used to identify the existence of these vortices (Hueso et al., 2023). This mechanism is driven by solar insolation, so it develops during the daytime due to the abrupt surface-air temperature change in response to the Sun's intense heating of the surface (Gebhardt et al., 2021) and references therein. When solar radiation heats the surface, a superadiabatic lapse rate forms in the lower part of the boundary layer, leading to an unstably stratified atmosphere and hence strong convection (Kahanpää et al., 2016). The differences in the surface-to-air temperature control the available energy to drive any dust devil which may form (Montabone et al., 2005).

A dust devil is known to extend on a vertical scale of up to the height of the convective boundary layer (Newman et al., 2002), reaching a few kilometers (Gebhardt et al., 2021) and references therein, the thermodynamic efficiency relates to how high (and hence how large and strong) dust devils can grow (Montabone et al., 2005). While on the horizontal scale, it extends to cover an area from a few centimeters to over a hundred meters (Newman et al., 2002). Generally, dust devils were observed to occur in all seasons in both hemispheres (Cantor et al., 2006). Peak activity occurs when the solar insolation peaks with large sensible heat fluxes (Gebhardt et al., 2020); this occurs during the southern spring/summer, with a moderate peak during the northern summer. Equation 1 explains that the dust devil activity (Λ) is roughly proportional to the surface sensible heat flux (F_s) and planetary boundary layer heat. η is the thermodynamic efficiency of the dust devil (Newman et al., 2002).

$$\Lambda \approx \eta F_s \qquad\qquad \text{(Equation 1)}$$

In recent studies, the Perseverance rover from Mars 2020 mission was designed to land and explore the Jezero Crater. The mission monitored the dust devils' activities in this region (Hueso et al., 2023). For the first 216 sols, the meteorological sensors on the rover observed, on average, over four convective vortices raised dust locally. While four passed the rover daily, over 25% were very dusty (dust devils) (Newman et al., 2022). An extended study covering more than 400 sols from the northern spring to northern autumn found a high abundance of vortex and dust devils at the Jezero Crater peaking at

noon. On average, the pressure data analysis revealed around 4.9 vortices per sol, with at least one in every five vortices carrying dust (dust devil). During a dust storm event, the dust devil became very frequent, where the air temperatures were warmer, and the differences in surface-to-air temperature were low (Hueso et al., 2023). Observation from orbital imaging has revealed that these dust devils exist at nearly all latitudes and form on all types of surfaces: from high elevations such as Arsia Mons (+17,250 m) to the bottom of Hellas basin (−8750 m) (Cantor, 2007). Despite these observations, specific regions on the planet tend to experience a higher activity of dust devils than others; Noachis, Thaumasia, Sirenum, and Arcadia/Amazonis regions (Newman et al., 2002). The latter are regions with planet-wide dust devil activity, both in terms of frequency of occurrence and size (large enough to observe) (Cantor et al., 2006). Whereas during the high dust loading period, the vertical surface-atmosphere temperature gradient and convection of warm air are thus reduced, which leads to obstruction of the growth of dust devils (Gebhardt et al., 2021).

1.4.3 Optical Depth

Dust is always present in the atmosphere, and its abundance varies significantly with the season and from year to year (Chen-Chen et al., 2021). Montabone et al. 2015 is a standard reference for studying the Martian dust climatology from 2005 to the present. In order to estimate the opacity of the atmospheric dust layer, the actual amount of dust can be measured using optical techniques from orbit or the surface. The vertically integrated (or column) optical depth is considered one of the critical physical parameters used to express and characterize the presence and spatial distribution of dust in the atmosphere over a period of time, as it is an accurate variable to account for the radiative heating and cooling effects of the dust. Knowing that is essential to study the dust behavior by producing estimations of dust mass mixing ratios and to describe the thermal forcing in the Martian atmosphere by calculating the heat rate due to absorption and scattering of solar radiation by dust (Montabone et al., 2015).

The retrieval of CDOD is produced based on observations of the Martian atmosphere obtained by nadir-viewing instruments, such as the TES aboard the MGS spacecraft, ACS Thermal Infrared channel (TIRVIM) aboard The ExoMars TGO

spacecraft, which had nadir observations of the Martian atmosphere and measured the column integrated opacities of dust at different times of day (Young et al., 2022), and EMIRS on board EMM also measures the column integrated dust (Amiri et al., 2022). In most cases, the opacity is provided at a given wavelength (e.g., 0.67 μm in the visible or 9 μm in the thermal infrared) (Forget & Montabone, 2017).

Both the amount of dust and the altitude it reaches are likely significant in determining the subsequent dynamics of a dust storm (Montabone & Forget, 2018). The effect of dust depends strongly on its vertical extent. In the case of a local dust storm, an opaque dust column restricted to around 10 km (the boundary layer) can cause a little effect beyond the location of the dust. The exact amount of dust (or even less) spread into the lower atmosphere for about 25 km will substantially affect the atmosphere's thermal and dynamic state (Kass et al., 2016). The vertical extent of dust varies strongly depending on the season and latitude (Montabone & Forget, 2018). Mainly, during large dust storms in the dusty season, at the equatorial and subtropical latitudes, dust height can reach around 60 -70 km (Clancy et al., 2010). In some global events, dust can loft up to 80 km altitude (Forget & Montabone, 2017). On the other hand, during the clear (non-dusty season), dust is mostly confined at high latitudes near the polar during the northern winter (Battalio & Wang, 2019).

1.4.4 Seasonal Variability

The amount of dust distributed in the Martian atmosphere is characterized by large spatial, seasonal, and interannual variations. Based on the observation of albedo on Mars, the distribution of mean surface dust is generally invariant over the long term, with some seasonal to annual variation (Newman & Richardson, 2015). The Martian climate and atmosphere exhibit a pronounced annually repeating seasonal variability, including CO_2, water, and dust cycles (Gebhardt et al., 2021) and references therein. A study by Bruce A. Cantor in surveying dust storm activity within a 2000 km radius of three sites on the planet: Columbia Hills, Northeast Syrtis, and Jezero over seven consecutive Martian years (MY 28 – MY 34), concluded that a total of 1321 dust storms (1228 local, 93 regionals) were observed on the specified areas. These storms were found to occur during all seasons but showed distinct seasonal trends (Cantor et al.,

2019). The number of storms, timing, locations, size, and extent show significant variations. However, despite the complexities of the Martian atmosphere, there are preferred periods and regions, generally repeatable from one year to the next (Kass et al., 2016). The MYs show two distinctive seasons concerning atmospheric dust loading (Montabone & Forget, 2018). Based on a comparison of multi-annual zonal means of CDOD, there is a "low dust loading" season between Ls 10° and Ls 140° and a "high dust loading" season at other times commonly referred to as the "dust storm season" (Montabone et al., 2020) as shown in Figure 4.
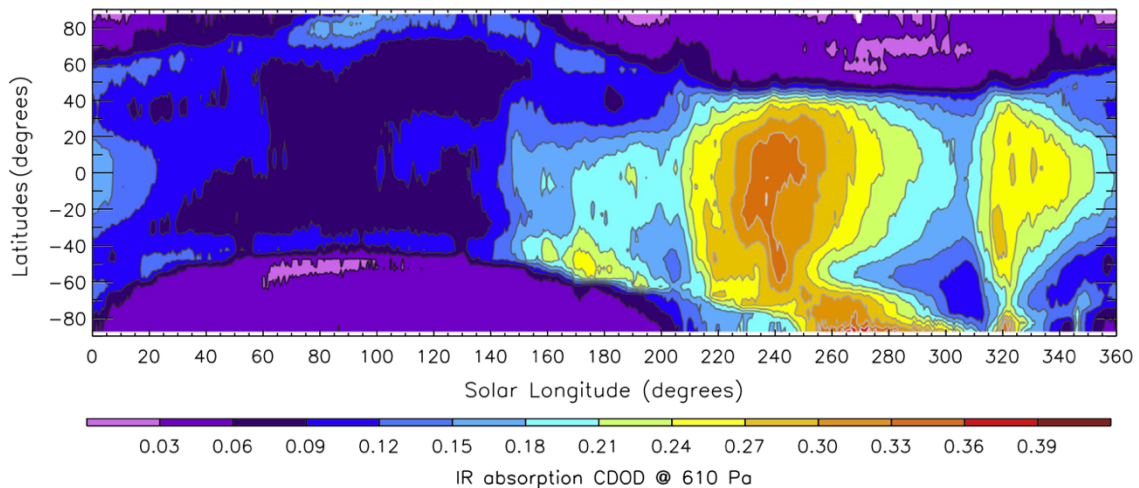
Figure 4: The zonal mean of the 9.3 lm absorption column dust optical depth from Martian year 24–31 excluding the years with global dust storm MY 25 and 28. Illustrate the two seasons concerning atmospheric dust loading (Montabone et al., 2015)

Like Earth, Mars's spin axis is tilted with respect to its orbital plane, so the planet has four seasons (see Table 1). Moreover, based on the planet's position with respect to the sun, these seasons can be measured in degrees of areocentric Solar longitude (Ls). In the northern hemisphere, the spring equinox occurs at Ls 0°, the summer solstice at Ls 90°, the fall equinox at Ls=180°, and the winter solstice at Ls 270°. Whereas it reversed in the southern hemisphere. Thus, the spring equinox occurs at Ls 180°. The length of Mars's seasons is unequal because of its large orbital eccentricity (0.093) (Cantor et al., 2001). The time around the aphelion, the planet's furthest point to the sun along its elliptical orbit, coincides with Mars's northern hemisphere spring and summer seasons.

During this period, relatively lower amounts of dust are present in the atmosphere. Large dust storm events are unlikely, while local dust storms may still occur (Gebhardt et al., 2020). While the time around perihelion, the planet's closest point to the sun along its elliptical orbit, coincides with Mars's southern hemisphere spring/summer, which is the Mars dust storm season (Gebhardt et al., 2021). Several factors drive the dust activity in these two seasons; the main one is the Martian hemispheric dichotomy in topography (Toigo et al., 2002). Where the southern hemisphere is several kilometers higher than the northern hemisphere, hence enhancing the atmospheric circulation and causing strong surface dust lifting and transport (Gebhardt et al., 2021). Another factor is the significant increase in insolation (Kass et al., 2016). The atmosphere is relatively warm and dusty, and this extra heat pouring into the southern hemisphere originates more significant turbulence and causes stronger thermal contrasts (Richardson, 2002), which provides high surface wind stresses (Toigo et al., 2002), allowing the air movements to readily lift the dust particles from the surface, stirring up the largest storms (Richardson, 2002). Fedorova et al. (2014) pointed out that during high dust loading conditions, larger sizes of dust particles have been observed between reff = 1.8– 3.5 µm (reff is the effective radius of the dust size distribution). Generally, Martian Atmospheric dust disturbances range in size from small local dust storms to regional storms and finally to planet-encircling global dust storms all over Mars (Rafkin, 2009). According to Cantor et al. (2001), the criteria of dust storms taking longer/shorter than three days and having an area larger/small than 1.6 million square kilometers are equivalent.

Table 1: Martian seasons (Cantor et al., 2001)

Seasons		
Ls	Northern	Southern
0°-90°	Spring	Fall
90°-180°	Summer	Winter
180°-270°	Fall	Spring
270°-360°	Winter	Summer

1.4.5 Local and Regional Storms

Most storms on Mars are local. They commonly occur at any time of the year (Toigo et al., 2018). Despite the fact it's frequent and repetitive, only a few of them have been studied with in situ data, and still, the effects they make on the atmosphere need to be well quantified (Ordonez-Etxeberria et al., 2020). Cantor et al. (2001) identified local dust storms as actively lifting dust particles over an area smaller than $1.6 \cdot 10^6$ km^2 during less than three sols. The same study (Cantor et al., 2001) claims that it was hard to observe and analyze this type of storm earlier due to the previous spacecraft's lack of spatial and temporal observations, which had limited coverage of the planet daily, besides the low spatial resolution. Overall, this kind of dust storms occurs due to enhanced local winds due to local topographical slopes, baroclinic waves, polar cap sublimation, and regional variations in thermal inertia (Cantor et al., 2001).

Regional storms have been observed in almost all recorded Martian years (Newman et al., 2002). Usually, regional dust storms are not exactly alike. Yet, several storms are noted to follow specific patterns and can be differentiated according to their onset location, evolution, and season of occurrence (Newman & Richardson, 2015). Three major seasonal types appear with the same behavior every MY, labeled as A, B, and C storms (can be seen in Figure 4). Usually, the first type (A) occurs around the middle southern spring covering the southern hemisphere and lasts for a moderate duration. This type affects the atmosphere by warming it up at most latitudes. Whereas B storms mostly initiate just after perihelion during a perturbed atmosphere near the southern polar and last for a long time each year. Finally, the C storm considered the shortest among all, starts after the end of the B storm every year in the southern hemisphere (Kass et al., 2016). The intensity and duration of regional dust storm activity vary depending on local atmospheric conditions like wind speed and seasonal variations in solar radiation received at different locations across Mars' surface (Wang, 2003).

Based on (Cantor et al., 2001), distinguishing the difference between local and regional dust storms is purely based on defined threshold values; regional dust storms are single events that actively lift dust particles over an area larger than $1.6 \cdot 10^6$ km^2 starting as smaller local events and then evolve over about period more than three sols (and

usually less than 20). Originally, around 50% of the regional dust storms formed due to minor local dust storm mergers. Temperature, as well as atmospheric circulation patterns, are other reasons for the formation of these storms. These events have more frequent activity during the warmer seasons when temperatures are higher and atmospheric circulation patterns are more active (Wang, 2003), as they have been observed mostly in southern spring and summer, from Ls 180° to 360°. Over the period MY 24 to MY 30, a total of 65 regional dust storms were observed by MGS-MOC and MRO- MARCI. These storms tend to occur in distinctive areas of the planet. Locations of preferred storm origination emerge from these observations include Acidalia (where the most dust storm originate), Utopia, Arcadia in the northern hemisphere, and Hellas, the most preferred region for the southern hemisphere (Wang & Richardson, 2015).

1.4.6 Global Storms

Global dust storms are the rarest and largest dust events (Cantor, 2007), considered Mars's most significant meteorological phenomena. These planet-encircling storms expand to cover all longitudes over a large latitude range involving both hemispheres in the planet, affecting the zonal and global-scale weather and variability of the whole Martian atmosphere by causing significant perturbations in air temperatures or opacities (Newman & Richardson, 2015). One global dust storm alone can produce high dust visible optical depths (typically larger than three and up to 10), generally, all over the planet. As a result, this thick global dust haze completely obscures the surface features of Mars from orbit, except for the poles, for several months (Bertrand et al., 2020). Unlike other storms, the interannual sequence of the global storm occurrence is irregular (Montabone et al., 2020). These storms occur only every few Martian years (MY) (Bertrand et al., 2020). This irregularity is likely controlled by the fact that the surface dust is redistributed consistently by various dust events such as dust devils, local and regional storms, as well as global-scale storms. After a global dust storm, the dust surface reservoirs must be refilled somehow (Battalio & Wang, 2019). The spatial distribution of the dust available for lifting plays a significant role in the occurrence of global dust storms. It determines whether or not a global storm may occur in a given MY.

A series of studies investigated global dust storms and found a strong connection between the changes in the orbital motion of Mars with the occurrence of global dust storms. The orbit-spin coupling hypothesis identifies a torque on the Mars atmosphere that varies strongly with time, and all of the Martian global dust storms developed when orbit-spin coupling torques are peaking and near times when torques are changing most rapidly (Shirley et al., 2020). During the last Martian decade (MY25 to 34), which is equal to two Earth decades from 2000 to 2019, only three global dust storms occurred: an equinoctial event in MY 25, a solstitial event in MY 28, and another equinoctial event in MY 34 (Montabone et al., 2020).

Global storms are developed during Mars' dusty season, southern spring, and summer (Bertrand et al., 2020). All the earliest global storms (before MY 25) lasting for more than 120 sols were observed to begin at either (Ls~200°–210°), which is called an "equinoctical" storm, or near solstice (Ls~260°–270°) called "Solsticial" storms (Newman & Richardson, 2015). Most likely and based on the observed and tracked such storms, they are characterized by several regional-scale storms coinciding (Montabone et al., 2020). This conjunction usually happens with cross-equatorial regional storms (Cantor et al., 2019). Based on that, these events do not have a single dust-lifting center(Cantor, 2007); instead, they develop as a result of the merging and combining of several active regional dust storms at low latitudes (Gebhardt et al., 2020).

1.4.7 Mars Topography
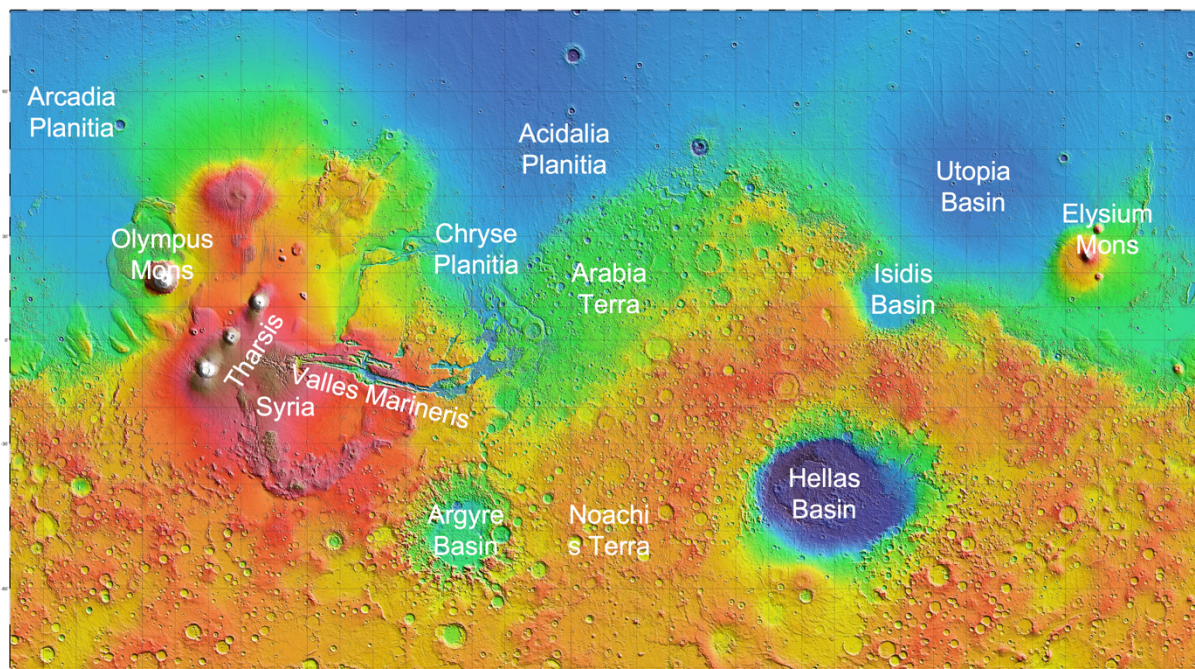
Figure 5: The topography of Mars by the Mars Orbiter Laser Altimeter MOLA (NASA Image Gallery)

Based on the Martian dust observations, there is a correlation between dust accumulation and surface topography (Martian topography in Figure 5). They are an essential parameter that affects dust-lifting activities (Basu, 2004). Prior simulations suggest that Mars's atmosphere contains topographic circulations that work efficiently in lifting the dust, and their contribution exceeds the contribution of the general circulation locally (Heavens et al., 2015), as lifting is affected by the sharp topographic gradient like how the terrain change from the Amazonis lowland to the heights of Olympus Mons and the Tharsis plateau (Basu, 2004). Most surface wind stress and circulation patterns changes are due to the topography impacts. Toigo et al. (2012) state that there is a strong correlation between topography and dust lifting by wind stress. The increase in the wind stress threshold leads to more dust lifting. The extensive topographic range, along with the thin atmosphere, results in significant effects that are manifested on a small scale in up-slope/down-slope, sea breeze, and deviations on near-surface winds, and on a large scale in generating gyres with strong boundary currents (Toigo et al., 2012). Wang and Richardson (2015), Montabone and Forget (2018) and Battalio and Wang (2021) agreed

on the preferred locations of origination of regional dust storms, which are Hellas, Acidalia, Utopia, and Arcadia Planitia. They appear to begin in association with cap winds or baroclinic fronts, then travel or expand primarily to regions of higher topography (Newman & Richardson, 2015); they are called "cross-equatorial dust storms" (Montabone & Forget, 2018).

We can say with some certainty that there is a strong association between dust storm distribution and topography in the northern hemisphere (Cantor et al., 2001). There is an active belt of dust-lifting centers in the mid-latitude and near elevated topography, such as Olympus Mons, the Tharsis Montes, Alba Patera, and Elysium Mons (Gebhardt et al., 2020). Cantor et al. (2001) reported a "statistically significant increase in the number of dust storms for the lowest elevation region" and "47% of the storms (108) occur in regions where the elevation difference is >2000 m over 5°" pointing to storms developing northwest Elysium. Other regions ranging from 250 – 1000 m experienced 71 local storms northwest of Olympus Mons, aureole, and western Arcadia. A small fraction of 14 storms in areas less than 250 m is found in the flat plains of Acidalia. Whereas the southern hemisphere is characterized by various terrains several kilometers higher than the northern hemisphere terrain. That played an essential role in enhancing the global overturning circulation, which coincided with stronger surface dust lifting and transport (Gebhardt et al., 2021).

As common, Martian global dust storms tend to originate in the southern hemisphere, especially Thaumasia, and general regions of Hellas in mid-latitudes that appear to dominate (Newman & Richardson, 2015). Besides Argyre basins and the polar regions, these are special zones on Mars as they are the overall dustiest locations on the planet for most of the Martian year (Forget & Montabone, 2017). The increased dust lifting in these regions is due to higher surface pressure, resulting in stronger winds and corresponding lower friction velocity thresholds (Rafkin, 2009). Specifically, based on values of the multi-annual TES mean, it is common to observe dust storms in Hellas regions. The basin is a huge deep crater about -8 km down and has a steep slope with respect to surrounding areas. The steep topography of the western and southern basin's rims is where the storms likely grew (Chow et al., 2018). And the reason for that is the combination of seasonal, slope, and cap edges winds produce strong flows (Newman &

16

Richardson, 2015). In other words, the formation of slope-wind circulation and the significant contrast in surface temperature between the southern edge of the basin and the CO2 ice-covered south polar cap (Strausberg, 2005). During the late spring and early summer, the lifted cold air from the polar caps meets the highly heated near-surface air producing steep lapse rates (Rafkin, 2009).

1.4.8 Effect of Dust on the Martian Atmosphere

Dust is a source of strong atmospheric radiative forcing (Montabone et al., 2020). When radiation travels through the atmosphere, its propagation is subject to interactions with atmospheric constituents (such as gases, clouds, and aerosols) and the surface. This physical phenomenon is known as atmospheric radiative transfer. Three interactions may occur when incident radiation hits a particle in the atmosphere: Firstly, the radiation absorption by a particle corresponds to an attenuation of the incident radiation through energetic modification such as internal heating or chemical reaction. Secondly, the emission of radiation if the particle is at the same wavelength as the incident radiation, or thirdly the radiation scattering by a particle which corresponds to an attenuation of the incident radiation by deviation in other directions than the original radiation trajectory (Vidot, 2014). This process impacts the atmospheric thermal and dynamic state (Montabone et al., 2005) because the thin atmosphere allows optical radiation to reach the surface (Haberle, 2003), and the dust particles are radiatively active, so they will absorb solar radiation and absorb/emit infrared radiation (Gebhardt et al., 2020). The existence of airborne dust in the Martian atmosphere, with its long exposure to solar radiation, leads to different effects depending on the intensity of the suspended dust in the air (Gebhardt et al., 2021).

In particular, the global dust storms and the subsequent high dust loading accompanying them have the strongest effects as they inject a large amount of dust particles into the atmosphere producing perturbations of temperature and density structure (Cantor et al., 2019), which propagate from the lower to the upper atmosphere, including the lower thermosphere, the ionosphere, and the magnetosphere (Montabone et al., 2020). These effects can last over several months (several tens of degrees of areocentric solar longitude, LS) below 60 km altitude in the lower atmosphere

(Montabone et al., 2005). Meteorological observation of the last three global dust storms (MY25, MY28, MY34) showed an impressive effect on atmospheric temperatures (Montabone et al., 2020). A specific detailed example observed by the Curiosity rover reveals that the local optical depth reached 8.5, the incident total UV solar radiation at the surface decreased by 97%, the diurnal range of air temperature dropped by 30 K, and the semidiurnal pressure tide amplitude increased to 40 Pa (Montabone et al., 2020) and reference therein: Guzewich et al. (2019).

The effects of the suspended dust in the atmosphere, generally, and the planet-encircling dust storms, mainly, are evident not only in the atmospheric thermal changes but also in the dynamic state of the atmosphere. Heating the dusty air and cooling down the surface (Gebhardt et al., 2020) will create differences between dusty air and clean air can reach more than 35 degrees Celsius (Webster, 2016). This high thermal contrast drives dynamic processes (Gebhardt et al., 2020) by altering the atmospheric circulation and the CO2 as well as water cycles (Bertrand et al., 2020). Overall, the global atmospheric circulation is enhanced in these conditions. A more vigorous circulation will lift more dust (Kass et al., 2016), creating positive feedback for the sustenance of the storm for several sols (Montabone et al., 2005). Notably, the positive feedback strength may change from place to place (Gebhardt et al., 2021).

1.4.9 Albedo

Albedo is used to describe how well a surface reflects sunlight (Christensen, 1988). The solar albedo is the ratio between the reflected and received flux over the whole solar spectral range. Both the spatial distribution and the magnitude of the surface albedo consider necessary for the characterization of the Martian surface and Atmospheric circulation (Wells et al., 1984). Figure 6 displays the surface albedo of Mars during the end of the southern winter in year 14 of the Gebhardt et al.(2020) simulation (details about the numbering in 2.4).
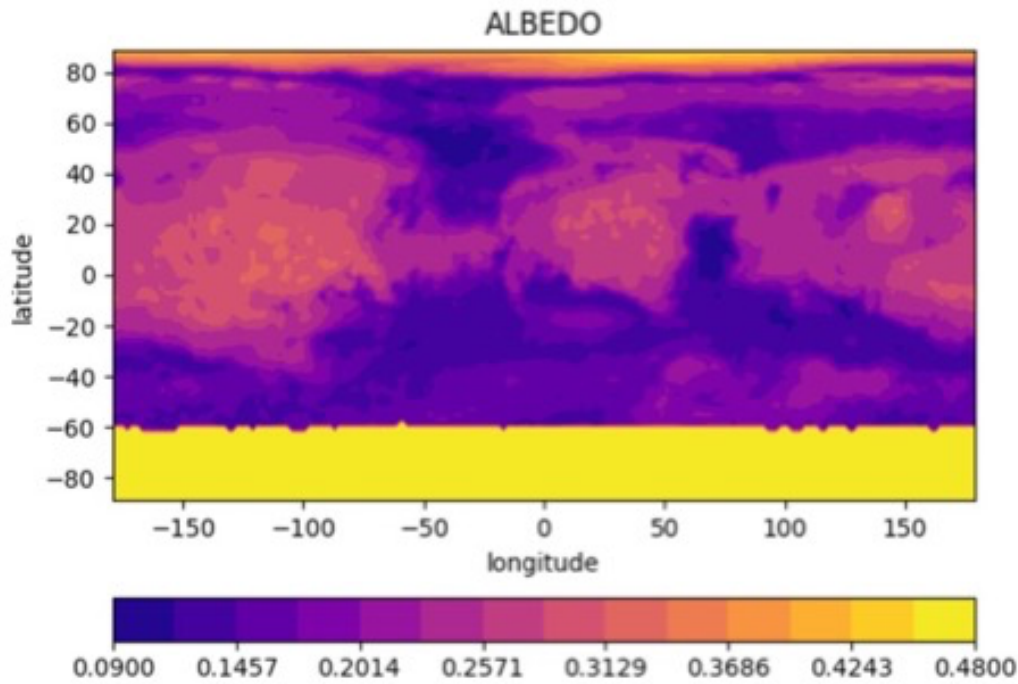
Figure 6: The MarsWRF model Martian surface albedo during the end of the southern winter, the feature shows the contrast between the brightness and darkness in adjacent areas.

The MarsWRF surface albedo changes because of the polar ice cap. During this period of the year, in southern winter, the southern ice cap is at its maximum accumulation, where the cooler temperatures increase ice cover. As a result of the obliquity of Mars's orbit, the southern pole is experiencing total continuous darkness, while the northern one is the opposite, with continuous sunlight. In this case, the north cap starts to recede and sublimate while the south grows and freezes, as in Figure 7. The sequential mechanism of exchange of CO2 between the atmosphere and the polar caps controls the atmospheric pressure to stay roughly constant over the year (Kelly et al., 2007). In the meantime, the fine-grained CO2 and water frost in the southern ice cap cause temporary, high albedo brightening (Byrne et al., 2008), given the fact that ice is a very reflective surface, as shown in Figure 6, where it exceeds ~0.4.

While observing the surface of Mars, H. Flaugergues (1796-1806) noted yellow clouds obscuring surface albedo features; these clouds were then identified as dust storms (Cantor et al., 2001). One of the visual criteria used to detect the occurrence of a dust storm is the daily variation in the visibility of the surface albedo observed by the

daily global maps. Giving an example to illustrate, on Earth, bright and dark regions almost have equal brightness on a cloudy day but not on a clear day; this implies that brightness differences in areas are associated with the atmosphere's optical depth (Petrova et al., 2012). This is consistent with (Christensen, 1988), who suggests that an albedo with a value from 0.3–0.32 indicates a thick layer of dust.

Several months of study by (Cantor et al., 2001) covered the dust storm season for the year 1999. Many storms were observed during this time, varying between local and regional storms. There is a notable increase in the number of storms in the intermediate surface albedo regions (between 0.20 and 0.27). Besides, most of the northern hemisphere storms clump in the borders of small local albedo features because the local albedo features are near the bottom of large-scale regional slopes. There is an obvious relationship between the albedo, thermal inertia, and topography. It is found that the thermal inertia is inversely proportional to the albedo, and the elevated topography is characterized by low thermal inertia. This positive correlation suggests that the generation of dust storms is associated with regional thermophysical characteristics (albedo and thermal inertia), topography, and other factors. Through various observations of the Martian surface, decadal changes in the surface albedo have been detected (Vincendon et al., 2015). These changes are primarily due to the removal and deposition of small amounts of the relatively bright dust on the surface over the larger-grained darker underlying material (Fenton et al., 2007). This modification is likely to occur because of dust erosion, which results from short-lived strong winds, dust devils, and dark sand saltation.
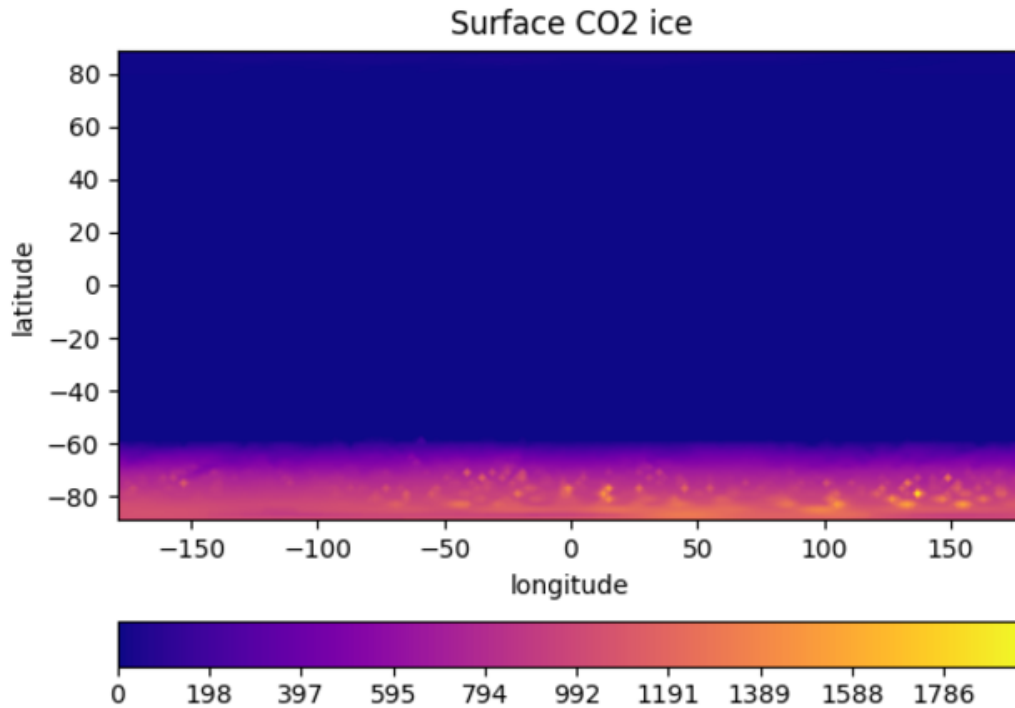
Figure 7: The MarsWRF model Martian surface CO2 ice in a unit of kg/m^2 during the end of the southern winter at Ls 186° sol 385 in the year 14 of the followed simulation, the feature shows the southern cap covered with ice.

1.4.10 Studying the Atmosphere and Forecasting the Storms

Dust considers a source of hazards for the spacecraft's entry, descent, and landing maneuvers, obstruction to operations done by solar-powered surface assets, and a threat to future robotic and human exploration (Montabone et al., 2020). The process of EDL of a spacecraft during the activity of a dust storm is risky, as it will reduce landing accuracy, which is caused by the strong winds and poor observing conditions associated with dust storms (Cantor et al., 2019). Therefore, it is crucial to understand the planet's conditions before planning the mission to ensure the safety benefits. There are various approaches for studying dust events on Mars; analysis of dust observations from satellites and rovers, numerical simulations models from MGCMs, and data assimilation techniques (Montabone et al., 2020). The latter combines all available information from observations and numerical models (Montabone & Forget, 2018), providing a complete, balanced, four-dimensional best fit to the atmospheric state, including the non-direct

measurements by spacecraft, such as wind and surface pressure (Montabone et al., 2005), which makes this approach a promising technique for forecasting Martian dust storms that could be potentially hazardous.

Scientists and researchers are making progress in understanding the interannual variability of dust events and how they affect the global climate; this will allow them to recognize the patterns and categories of dust storm events on the planet (Webster, 2016), which helps improve predictability. Mainly, temperature and aerosol observations are essential variables in the prediction process. The ability of the numerical models to simulate the proper environment and condition of transporting dust (Montabone & Forget, 2018) with the assimilation of the thermal profiles and dust opacity can lead to predicting dust evolution days in advance (Montabone et al., 2005). Compared to visible dust, the temperature profile can give some regularity in large dust storms. Thus, the clearest way to study and interpret the seasonal patterns of Martian dust storms appears to be captured by measuring the temperature (Webster, 2016).

1.4.11 Synthetic Satellite Images

Before the availability of data from satellites, representative images are required. It is possible to produce images close to those received from future satellite instrumentation. A possible method to do this is to use data from existing operational and experimental satellites; this method produces simulated imagery. Another technique involves using numerical models, which produce synthetic imagery (Grasso et al., 2008).

Output from numerical models can be used to generate synthetic satellite images by using a forward model able to compute the top-of-the-atmosphere reflectance for a given band. The forward model refers to a radiative transfer model RTM that considers surface, atmospheric, and cloud properties and predicts what radiance and brightness temperatures a satellite will observe. The procedure for generating synthetic satellite imagery was developed at the Cooperative Institute for Research in the Atmosphere (CIRA) over the past few years. The use of synthetic satellite imagery provides a new and unique method of evaluating and characterizing the high-resolution model output. It also gives a comprehensive view of the atmosphere that provides a quick analysis of model output fields and allows for efficient identification of important features of the

weather conditions and their evolution (Bikos et al., 2012). Meteorologists and scientists on Earth use weather prediction models for short- and long-term weather forecasts. The models can generate forecasts that provide information on temperature, precipitation, wind, and other weather conditions at specific locations, as well as more general information about weather patterns. Synthetic satellite imagery can also be used for numerical weather prediction verification by comparing synthetic imagery from a forecast model to observed imagery (Grasso et al., 2008), leading to higher or lower forecaster confidence in the model solution. Forecasts and synthetic satellite images in near-real time were produced hourly, from 9 to 36 hours into the forecast period, in collaboration with NSSL and WRF-ARW. Using a similar methodology that followed in this project, WRF-ARW outputs from NSSL were used as inputs to a forward radiative transfer model to generate synthetic GOES-R ABI imagery (Bikos et al., 2012). Derived Product Imagery (DPI) can be obtained by combining the images obtained from GOES-R ABI. DPI has various applications in detecting different events, such as low clouds consisting of liquid water, fog, and skin temperature (Grasso et al., 2008).

Chapter 2: Methods

This chapter is divided into four sections: The first section introduces the model MarsWRF. The second section presents the model output variables used in the project. After that, the radiative transfer model & DISORT modules setup are mentioned in detail in the third section. Finally, the T15 Mid-level atmospheric temperature curve used as an indication of a dusty atmosphere is discussed in the fourth section.

2.1 About the Model

Generally, atmospheric models are a necessary tool to enhance our understanding of the Martian atmosphere. In order to achieve the primary goal of this project, the work involved using two models; the MarsWRF model played an important role as the primary source of input data. These data are passed through a radiative transfer model that can compute realistic radiances for different spectral bands. The terrestrial model WRF is a numerical weather prediction (NWP) and atmospheric simulation system for both research and operational applications. A collaborative effort of building and developing WRF was done by multi-agency, including the National Center for Atmospheric Research (NCAR), the National Oceanic and Atmospheric Administration's (NOAA), Earth System Research Laboratory (ESRL), and others (Skamarock et al., 2008). Initially, the model was not configured such that a fully global domain could be simulated and was written and designed to be exclusively applicable to the Earth (Richardson et al., 2007). However, it is maintained and supported as a community model to facilitate wide use internationally for research and teaching (Skamarock et al., 2008).

A Mars version of WRF is a part of the PlanetWRF models for planetary atmosphere research. The model is a Mars General Circulation Model (MGCM) that is developed to understand and simulate the behavior of the Martian atmosphere and surface for many MYs (Richardson et al., 2007); by filling the spatial and temporal gaps in observational coverage and providing predictions for atmospheric fields that cannot be observed directly like winds (Gebhardt et al., 2020) and references therein.

The starting point of this project is the existing MarsWRF model data from Gebhardt et al. (2020). In the mentioned study, the applied MarsWRF model version 3.3.1 was set up in grid resolution of 2° × 2° and 45 vertical levels throughout 10 MYs. The Gebhardt et al. (2020) model grid staggering is a vertical grid structure with equidistant vertical pressure levels, resulting in the vertical resolution increasing from the model top to bottom in terms of altitude. This version of the model has a dust cycle but doesn't has a water cycle, so there are no effects from water clouds, only dust clouds.

A challenge appears for MGCMs regarding dust events. As global dust storm events occur in some MYs and are absent in others, the model had to produce these events in a few but not all MYs. The local, regional, and global dust storms can be produced with different techniques that allow the model to deal with dust in a self-consistent manner and include various dust storm events, e.g., interactive-dust-lifting techniques. The used model was run following the latter technique with an infinite surface dust reservoir supply. This means that dust is completely freely lifted from the surface, transported through the atmosphere, and deposited back onto the surface with an inexhaustible amount of available surface dust. Among all the simulations performed using the interactive-dust-lifting technique, this model runs best matches the occurrence of global dust events in some MYs and their absence in others (Gebhardt et al., 2020).

The model's ability to generate local, regional, and even global dust storms depends on setting suitable model parameters controlling surface dust lifting. Global models have parametrization schemes used for processes that the model resolution cannot resolve. The radiation scheme used in the model is a k-distribution radiative transfer model to detect the change in dust and capture dust-radiation feedback. The model runs with fully interactive dust lifting, which is based on one scheme for dust gravitational sedimentation and two model parametrization schemes for surface dust lifting, the first is the dust devil lifting, and the second is wind stress lifting, which depends on threshold wing stress, wind speed, and air density.

After several test runs of the model with different surface dust lifting parameters to determine the best match between modeled and observed T15 temperature, Gebhardt et al. (2020), used the following values of the 3 surface dust lifting parameters:

1. The first parameter is the dust devil lifting rate constant AlphaD αD $1.0 \times 10^{-9} kg\ J^{-1}$, which is a constant of proportionality between the amount of dust lifted by dust devils per area and time, the surface sensible heat flux, and the PBL (planetary boundary layer) thickness.

2. The second is the wind stress lifting threshold Tau $\tau = 0.0657625\ Pa$, which is the critical value of wind stress which must be exceeded for saltating particles to start ejecting surface dust.

3. The last one is the wind stress lifting rate constant AlphaN $\alpha N = 8.5 \times 10^{-5}$, which is the constant of proportionality between the vertical flux of dust and the horizontal saltation flux of sand.

The work of Gebhardt et al. (2020) was built on previous models and studies following the same approach; Basu et al. (2004), Newman and Richardson (2015), Newman et al. (2019), and Richardson et al. (2007) who point out the possibility to use interactive or prescribed dust. Moreover, some observational data from the Mars Global Surveyor (MGS) using MOLA and TES instruments helped get the model's thermal inertia, albedo, and topography maps.

The MarsWRF data can be accessed through the output files of the model, which are named as follows: wrfout_d<domain>_<date>, where <domain> represents domain ID and is 01 everywhere in this thesis, and <date> represents a date string. These files are netCDF files (Network Common Data Form) that are used for storing and retrieving multi-dimensional data.

2.2 Model Variables

MarsWRF model output data are the primary source of variables in this project. These variables were read directly from the model output data, as shown in Table 2.

Table 2: List of different variables used from MarsWRF data with their dimensions and units.

	Variable	Source
1	XLONG is the Longitude coordinates in degree	
2	XLAT is the Latitude coordinates in degree	
3	vertical model coordinates:	
	o ZNU is the Altitude layers	
	o ZNW is the Altitude levels	
4	HGT is the Terrain height (3D) in meters	MarsWRF output
5	P is the Perturbation pressure (4D) in Pascal	
6	PB is the Base state pressure (4D) in Pascal	
7	P_TOP is the Pressure top of the model (1D) in Pascal	
8	PSFC is the Surface pressure (3D) in Pascal	
9	T is the Perturbation potential temperature (4D) in Kelvin	
10	TAU_OD is the Optical depth on full eta levels (4D)	
11	ALBEDO is the model albedo (3D)	

All variables' dimensions are consistent with the dimensions of the model grid. The MarsWRF vertical coordinate is the terrain following vertical coordinate eta. The vertical coordinate is available as full-layer values or mid-layer values; 46 vertical levels mean 45 vertical mid-layer coordinates. The altitude level ZNW consists of 46 levels (eta values on full (w)levels) quantities are computed at the top and bottom sides of a grid cell, while the altitude layers ZNU consist of 45 layers (eta values on half (mass) levels) (see illustration in Figure 8), the mass-related quantities such as pressure, temperature, and humidity are computed at the center of both horizontal and vertical grid cell and referred to as a mass grid. The levels distribute the model levels between the model top and the surface. Other dimensions are longitude with 360° and latitude with 180°. Some variables are in 3 dimensions (longitude, latitude, and vertical dimension), such as Perturbation pressure, Base state pressure, potential temperature, and Optical

depth, while others are in 2 dimensional (longitude and latitude), such as surface pressure and others.

(TAU_OD2D) dust optical depth in the function of longitude and latitude is another useful key from the MarsWRF variables that were used separately to plot column dust optical depth in order to extract the time, duration, and location of dust abundance in general and dust storms in particular. Based on the characterization of the dust optical depth, we can gain insight into the behavior of dust on the planet.; this will help us to determine the exact time and location of a dust event.
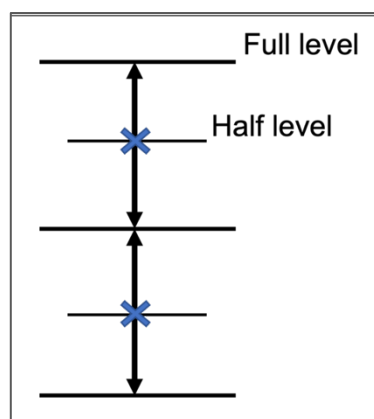
Figure 8: Illustration of eta levels; ZNU (eta values on half (mass) levels) with 45 layers and ZNW (eta values on full (w) levels) with 46 levels

On the other hand, some variables were not directly available in the MarsWRF output data, so some data conversions are necessary. The calculation and reconstruction are based on MarsWRF-ARW Users' Guide from National Center for Atmospheric Research. (2011) as follows :

$$\text{Total pressure} = \text{P+PB} \qquad \text{(Equation 2)}$$

Where the P is Perturbation pressure, and PB is Base state pressure.

$$\text{Potential temperature in K} = \text{Potential temperature } (\theta) + 300 \qquad \text{(Equation 3)}$$

$$\text{Absolute temperature } T = \theta \left(\frac{P}{P0}\right)^{\left(\frac{\mathcal{R}}{c_p}\right)} \qquad \text{(Equation 4)}$$

Where P is total pressure, P_0 is the surface pressure, R is the gas constant of air on Mars (192 J/kg/K), and c_p is the specific heat capacity at a constant pressure in Mars (730 J/kg/K)

    - To get the altitude

    1- convert eta to pressure at height h (Ph)

The eta coordinate $= \dfrac{(P - P_{top})}{(P_{surf} - P_{top})}$ where P_{top} is the pressure top of the model and P_{surf} is the pressure at the surface.

$$Ph = (eta\ value\ (P_0 - P\_top) + P\_top\ ) \qquad \text{(Equation 5)}$$

Eta value = ZNU to calculate the pressure height for every layer or ZNW the pressure height for every level. P_0 is the surface pressure.

    2- Calculate the altitude (h) using the barometric formula:

The barometric formula is the measurement of the air pressure in the atmosphere and how it changes with the altitude, pseudo-altitude $= P_0 e^{-\frac{h}{H}}$

$$h = \ln\frac{Ph}{P_0}(-H) \qquad \text{(Equation 6)}$$

where P_0 is the surface pressure, and H is the scale height of Mars = 11.1 km

2.3 The Radiative Transfer Model DISORT

Building upon this work, this project will generate synthetic satellite images of Mars dust storms. The method was based on the radiative transfer model DISORT, which is a numerical model developed at Atmospheric & Environmental Research AER, widely used for atmospheric sciences applications (Clough et al., 2005). Generally DISORT model is a scientific software package and one example of an accurate radiative transfer scheme. The model is used widely in performing radiative transfer calculations and solving problems in plane-parallel, vertically inhomogeneous media such as a planetary atmosphere (Stamnes et al., 2000), simulating radiative transfer interactions and atmospheric correction of airborne/satellite data & images and allowing for retrieving atmospheric composition. It was a helpful method for applying the MarsWRF output data and getting the synthetic satellite images of Mars dust storms. The model can

efficiently calculate fluxes and intensities at any specified angle and location within the specified medium. Lin et al. (2015) mentioned some background information about the DISORT model. The first version of DISORT, released in 1988, was able to calculate fluxes in an ideal way but produced less accurate intensities. The updated version (DISORT 2.0) released in 2000 increased the accuracy of intensities and included a more general bidirectional surface reflection distribution function as the lower boundary. According to Stamnes et al. (1988), the discrete ordinate algorithm for radiative transfer calculations can be applied from the UV through to the radar region of the electromagnetic spectrum. This model provides several important features; it is stable for a large number of quadrature angles and optical depths, offers a rapid computation of bulk albedo and transmissivity when there are no thermal sources, and allows for an arbitrary bidirectional reflectivity at the lower boundary; directional emissivity is computed from this reflectivity.

Generally, the model has been widely used in different kinds of software tools and packages. We perform the radiative transfer using the public domain discrete ordinates Python package DISORT pyRT_DISORT. It is a collection of different modules designed to run independently, which helps compute the arrays that DISORT needs (Kconnour.Github). In addition to the variables that were used directly from the MarsWRF output data and the variables that were calculated, some more variables need to be provided; these will be calculated from the DISORT modules.

Initially, the working process began with running a trial DISTORT model aimed to simulate reflectance spectra of the top of the atmosphere containing Martian dust as observed from an orbiter (Kconnour.Github). The resulting data represent the simulation of reflectance spectra wavelengths for the atmosphere. Based on the model's modules, we can move on to the next step by selecting the related parts of the model DISORT and building on them to develop our program with a selected variable from MarsWRF output files.

2.3.1 The Model Modules

1.   The observation module has 2 functions, one for pixel wavelength and the other for angles. The pixel wavelength is in microns, and the angles are incidence, emission, and phase angle.

2.   The equation of state module (Atmospheric gas) defines the altitude grid of the model. It contains data structures used to compute and hold a hydrostatic equation of state. All module inputs are used from MarsWRF output variables; altitude grid over which the eos variables are defined, pressure and temperature grid at all values in altitude grid. This module computes the number density and column density of atmospheric gas. Also, get the number of layers in the model and the scale height at the boundary altitude.

3.   After defining the boundaries used in the model, it's time to start building the model, which begins with the Rayleigh module. The inputs are pixel wavelength and atmospheric column density, and this module contains structures for creating atmospheric arrays for Rayleigh scattering, which are the optical depth, single scattering albedo, and Legendre coefficient decomposition phase function arrays.

4.   The aerosol module contains structures to create atmospheric arrays for dust that DISORT requires. According to Wolff et al. (2009), from the perspective of radiative transfer, three basic parameters need to be specified for each discrete altitude range: optical depth, single scattering albedo, and scattering phase function to build an aerosol model. The 3 output arrays:

-Forward Scattering contains a structure to store forward scattering properties (including the single scattering albedo). It's a function of particle size and wavelength.

-Vertically resolved Optical Depth, used from the output data of the MarsWRF and set at a spectral wavelength of 670 nm.

-Legendre Coefficients of the phase function.

Following the model simulation approach of Newman and Richardson (2015), Newman et al. (2019), and Gebhardt et al. (2020), the model dust particle size grid was set to be 4 μm. As the too-slow decay of global dust storm events is considered a known

MarsWRF shortcoming, a common practice is to run the model with this dust particle diameter (4 μm), including a dust sedimentation rate larger than in reality. In this module, there are tabulated values of absorption and extinction cross sections and phase function Legendre coefficients, they are a function of particle size and pixel wavelength, and they are interpolated to the pixel wavelength and dust particle size we used here.

Outputs from this module are the dust arrays, dust single scattering albedo, and dust phase function.

5.   The atmosphere module combines properties of Rayleigh scattering and scattering by dust aerosol, such as optical depth, single scattering albedo, and phase function. These parameters represent the total model.

6.   After creating almost all the model arrays, it's time to set some control parameters. The controller module includes several computational parameters that control how DISORT runs and performs basic checks that these values are reasonable. These Parameters hold the number of model layers, angles, levels, and streams. The latter variable is the quadrature angles which are used to evaluate the accuracy of flux and intensity and the computational efficiency. Generally, a lower number of streams (fewer than 16) will decrease the accuracy and affect the DISORT computation time, so in this project, 32 streams were used (Stamnes et al., 2000).

7.   The radiation module contains data structures for holding the radiation variables, the incident solar radiation at the top of the atmosphere, and the emission of thermal radiation.

8.   The output module creates some output parameters and arrays to define how DISORT will run. Mainly, it will provide the albedo of the medium array, the diffuse downward flux array, the diffuse upward flux array, the direct beam flux array, the flux divergence array, the intensity array, the mean intensity array, and the transmissivity of the medium output array.

9.   The surface module contains structures for making arrays of surface reflectance. The Lambertian phase function is used in this work.

Mostly, all input variables and output arrays of the modules (i.e., Rayleigh module, aerosol module, atmosphere module, part of the controller module, part of the output module, and surface module) were included in a loop run-over latitude and longitude. Summary of the modules shown in Table 3.

10.   The final step is running the model after getting all the input variables we need. Around 50 variables were set in the correct order in a loop as a last step to simulate the reflectance of the top of the atmosphere. The loop will run in steps of 2 degrees because of the model's horizontal resolution over latitude and longitude. Each point of longitude and latitude has all input data described previously and 45 vertical layers of altitude or 46 vertical levels, depending on the variable type. The input data on the altitude needs to flip, as the DISORT's convention assumed that the altitude starts from the top of the atmosphere, and it must be decreasing.

The final result is the UU variable, which is the mean intensity of the output array. It represents the reflectance of the top of the atmosphere for each longitude and latitude. Another essential step after running the loop is archiving and saving the output arrays of the top of the atmosphere inside a loop in 2 dimensions (longitude and latitude) for reusing the data, then extracting and saving the final output array UU as a npy file format. The data are saved as a .npy file containing the final output array, which will be loaded separately to plot the reflectance and get the synthetic satellite images of Mars Dust storms.

Table 3: Summary of the inputs and outputs of different DISORT modules.

Module	Aim	Input	Output
1. The observation	computing quantities required by DISORT	angular quantities	incidence, emission, phase angle
		spectral wavelength	670nm
2. Equation of state	define the boundaries that will be used in the model	Altitude, Pressure Temperature	Number density Column density
3. The Rayleigh	create atmospheric arrays for Rayleigh scattering	Pixel wavelength	Rayleigh arrays
		column density	
4. The aerosol	create atmospheric arrays for dust	Forward Scattering	Dust arrays
		Optical Depth	
		Legendre Coefficients	
5. The atmosphere	Combine information on atmospheric gas and dust	Rayleigh arrays Dust arrays	Model arrays: Optical depth Single scattering albedo Phase function
6. The controller	set computational parameters that control how DISORT runs	model layers, streams, levels, and angles	checks if values are reasonable
7. The radiation	Specify the flux and thermal quantities	Incident solar radiation at TOA	
8. Output	creates output parameters and arrays to define how model will run.	polar angles user levels azimuthal angles	albedo of medium array, flux arrays, the intensity arrays, and the transmissivity of the medium output array.
9. The surface	creating arrays related to DISORT's surface treatment	albedo, n_streams, n_polar, n_azimuth, user_angles, only_fluxes	arrays of the surface reflectance

2.4 T15 Mid-level Atmospheric Temperature

Generally, a match to observed dust optical depths does not necessarily mean a match to the actual radiative forcing since this depends on the dust radiative properties in the model, which may differ from those in the real atmosphere. While on the other hand, a match to the observed air temperature provides a realistic dust cycle as it creates genuine radiative forcing and circulation response, consequently, realistic surface dust

rearrangement (Newman & Richardson, 2015). Newman et al. (2019) points out that comparing modeled and observed T15 temperatures enable us to assess how realistic dust storms are. To differentiate the normal Martian atmospheric conditions from the global dust storm conditions, a bulk metric based on mid-level air temperature is used (the global T15 temperature curves) (Shirley et al., 2019). The term T15 temperature refers to temperatures measured in the 15μm CO_2 absorption band, which is sensitive to the amount of dust in the atmosphere and roughly corresponds to the altitude range from 10 to 40 km, weighted at ∼25 km and ∼50 Pa (Newman & Richardson, 2015). Using the T15 curve is the cleanest and simplest method of categorizing the size of a given storm in a simulation, a vital tool for sensitive measurements & the clearest pattern in the storms. Even more, it allows tens of simulation years to be presented and interpreted in one figure (Newman et al., 2019).

Figure 9 shows observation-based background global T15 temperature and that simulated by MarsWRF with the maximum measurement sensitivity. ca 25 km (Gebhardt et al., 2020). Following the dust storm, the classification scheme of (Newman et al., 2019) and based on observations, years with peak T15 more than 16 K higher than the background are categorized as global dust storm years. A possible global dust storm year if background values are exceeded by 10–16 K; otherwise, the Martian year is defined as nonmajor dust (T15 less than 10 K higher than the background).

T15 curve presents Gebhardt et al. (2020) numbering of years by the MarsWRF model run. The study of Gebhardt et al. (2020) focused on the 10 years, with the first year of the model run being discarded for reasons of model spin-up. Years 32, 33, and 34 … were numbered as Years 1, 2, 3, etc.…. According to the mentioned curve, global dust storm exists in years 9 and 14 with the maximum temperature measured between 205 and 210 K. whereas, in Years 5, 8, and 12, the maximum values of T15 are close to the background values, so no global dust storms occurred during these years.

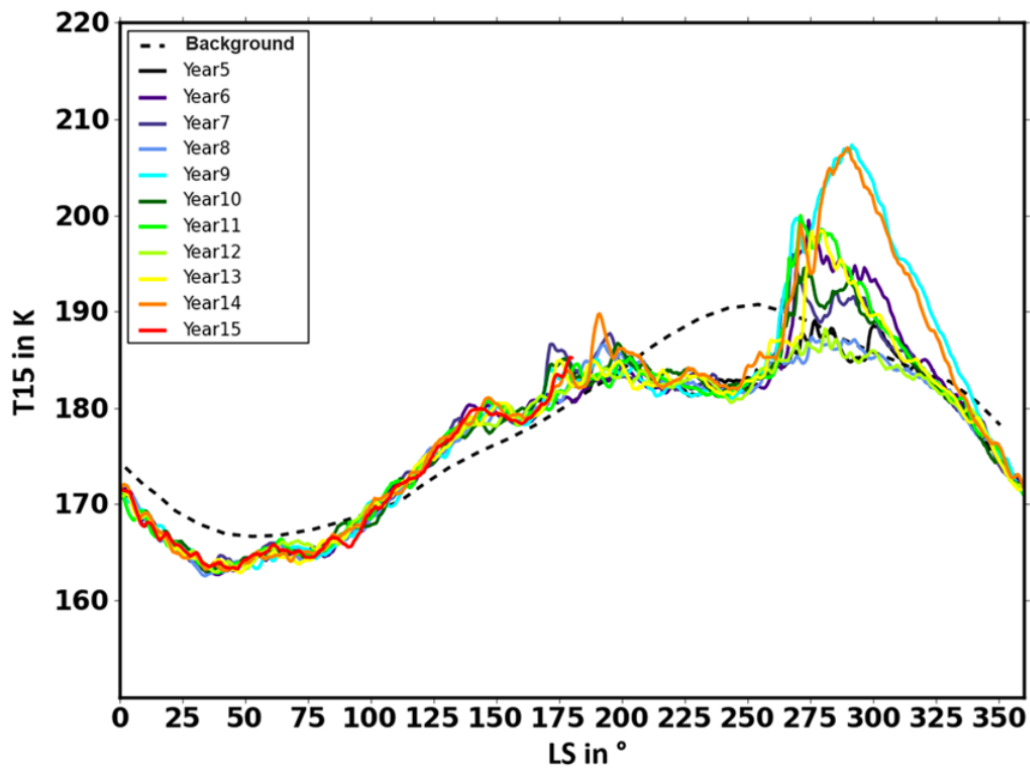Figure 9: Climatological background (black dashed line) and MarsWRF simulated global T15 temperature curves from the 2° × 2° model (solid lines).

This curve was selected entirely from (Gebhardt et al., 2020) Figure 3a. (solid lines) is MarsWRF simulated global T15 temperature curves from model runwith τ = 0.0657625 Pa, α_N = 8.5×10^{-5},and α_D = 1.0 ×10^{-9} kg J^{-1} shows 10 MYs.

Chapter 3: Results and Discussions

This chapter is divided into two main sections. The first section presents plots of column dust optical depth illustrating the evolution of a global dust storm. While the second includes two sub-sections, the first one discusses the obtained results of the synthetic satellite images in 670 nm for various dust events. The second compares synthetic images with dust optical depth and synthetic images with zero dust optical depth.

3.1 Dust Optical Depth

All years and sols in this paper follow the numbering of the Gebhardt et al. (2020) MarsWRF simulation run. The column dust optical depth plots shown in Figure 10 illustrate the MarsWRF-simulated global dust storm evolution in model year 14; the selection of the year was based on the T15 data from the model in Figure 9. Figure 10 shows selected sols, using 1 plot per sol allows us to explore the daily or the seasonal variability of dust activity in one MY. It also features other typical characteristics of the seasonal evolution of optical depth of global dust storms, such as large values at southern polar latitudes, whereas the northern high latitude regions are generally free of dust.

The overall opacity starts to increase monotonically at the onset of the dust event during Ls 263° in sol 507 of the model run. The dust begins lifting in the south of Chryse Planitia over a narrow portion of the equatorial zone. By the sol 516 Ls 270°, the optical depth with a value exceeding 5 covered wider regions near the equator and extended up to roughly 40° in the southern hemisphere. Column dust opacity measurements in this period sol 507-sol 516 around the south of Chryse Planitia Figure 10 (a, b) showed a steep increase from 1.6 up to 5.8 throughout nearly 10 sols. An intense dust activity occurs in the southern and northern of the Hellas basin in Ls 278° sol 529; this phase corresponds to a regional dust storm that develops and moves southwards and eastwards near the 20°S and 70°S. During sol 532 at Ls 279°, other dust lifting centers arise near Arcidalia Planitia 50°N north of Olympus Mons.
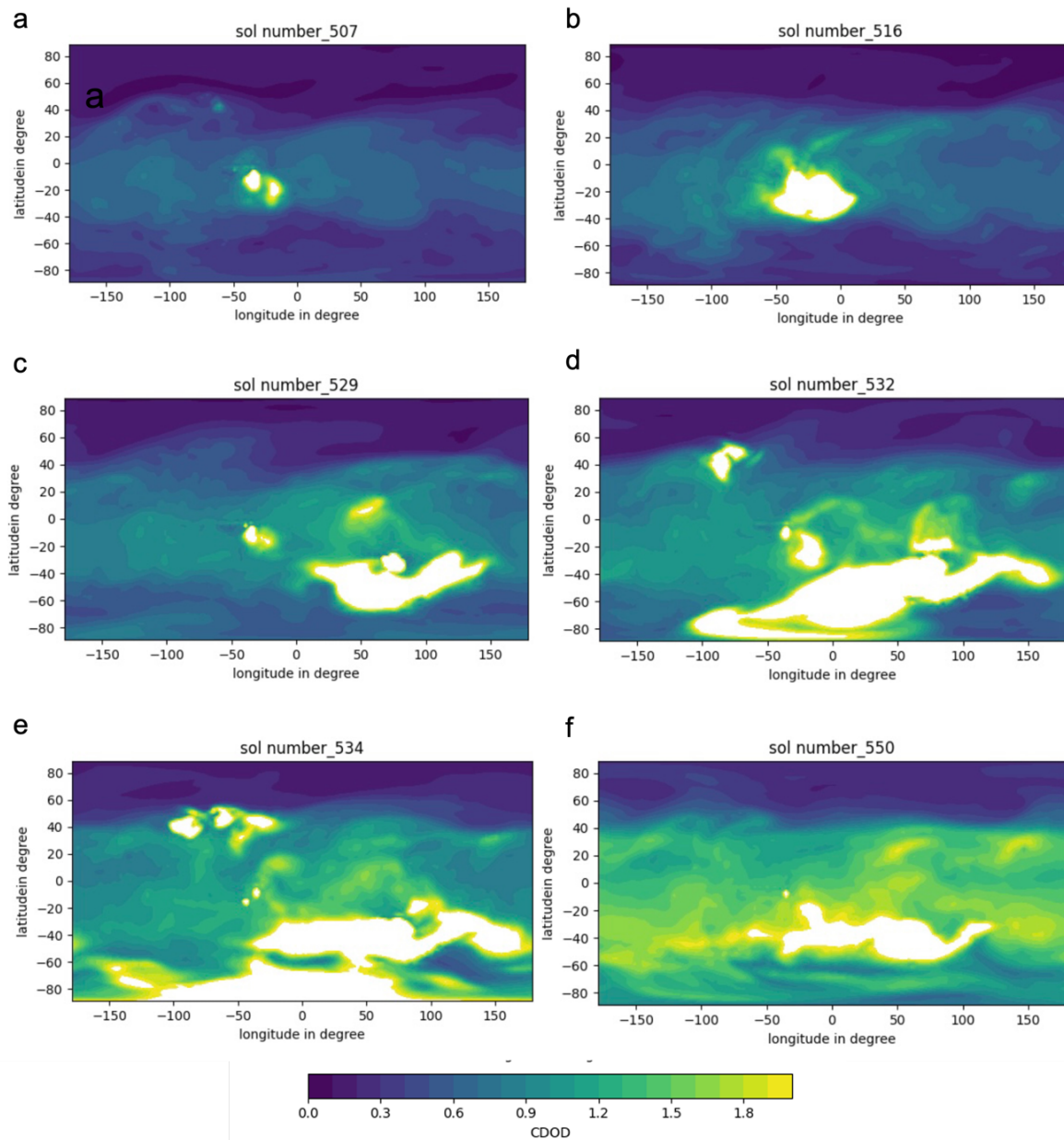
Figure 10: Column dust optical depth (670 nm) of the year 14 of the MarsWRF model run shows the global dust storm. Starting with (a, b) the onset of the storm, Ls 263° to Ls~270°, (c, d) the expansion phase Ls 278° to Ls 279°, (e) the intense phase Ls 281°, and (f) the decay phase Ls 291°.

The mentioned dust lifting centers are consistent with those observed by Gebhardt et al., 2020. In his study, Gebhardt labeled 4 surface dust lifting regions at equatorial latitudes, named SCP (south of Chryse Planitia), N-HB (northern Hellas Basin), S-HB (southern Hellas Basin), and N-OM (north of Olympus Mons). During sol 534 Ls 281°, the regional storm turns into a global storm, triggering the maximum amount of dust into

the atmosphere at all longitudes and from 50°N to the south polar 90°S with, generally, the optical depth value of over 3 in most of the planet and over 5.8 in the dust lifting centers. It only took ~30 sols to encircle the entire planet with a huge dust cloud. This mature storm stage is where maximum atmospheric dust loading and temperatures occur. Lastly, the global dust storm enters the decay phase in sol 550 at Ls 291°; there is almost no dust lifting, and dust starts settling out of the atmosphere.

3.2 Synthetic Satellite Images of Mars Dust Events

After running the DISORT model, this project's main results are synthetic satellite images of different Martian atmospheric conditions. Most importantly, these products contribute to adding values to the output data of the MarsWRF model because they can be used to evaluate and validate the model data. In general, one way to test the validation of synthetic imagery is by comparing them with real satellite images. Making the comparisons between model data and satellite images will work to support the technical specification of satellite instruments and refine numerical models of the Mars atmosphere. However, the model data in this work can't be used directly in the comparison process as the images represent one Martian year of the model run, not a real Martian year.

The model data must be converted into physical units of radiation of satellite images; that's why we used the radiative transfer model. In this case, the generated images must be similar and close enough to the real satellite images. By using the extracted result file that saved output data of the DISORT model, as described in the previous section, we were able to plot the top-of-the-atmosphere reflectance of Mars, producing $2° \times 2°$ grid resolution images, showing different atmospheric conditions and various phases of dust events on the planet. The output images are shown in the figures below store information in physically meaningful units representing the top of atmosphere reflectance. These reflectance values will include surface and atmospheric aerosol & gas contributions. In this work, the used model version includes physical process parameterizations specific to Mars, such as the carbon dioxide cycle and the dust cycle. However, the model doesn't have an active water cycle, so the TOA reflectance provides only information about the dust, making it consistent with this project's focus.

3.2.1 Small (Local) Dust Storms
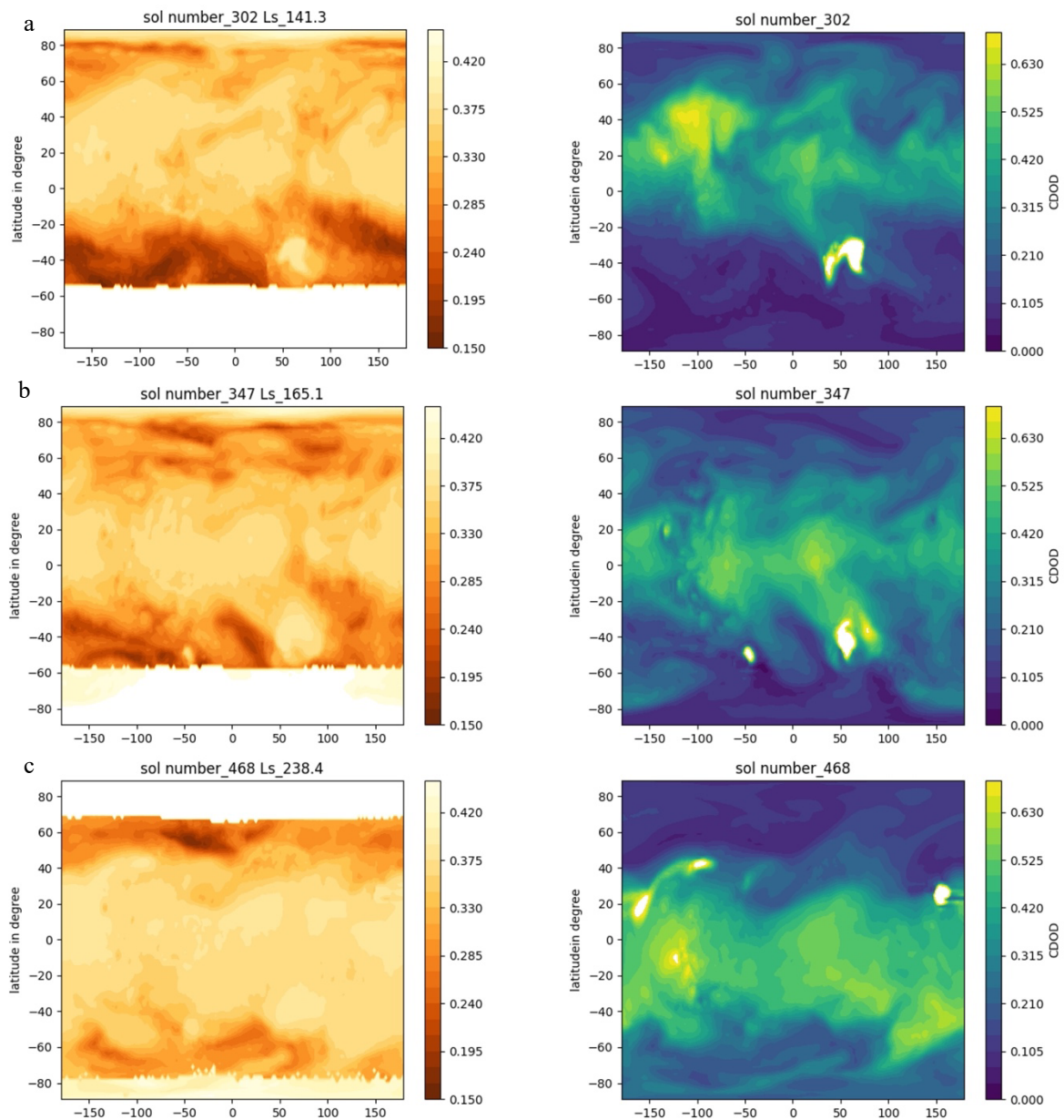
Figure 11: Synthetic satellite images (670 nm) in $2° \times 2°$ grid resolution showing the change in surface dust on a local scale. In MY14 of Gebhardt et al.(2020) model years at (a) Ls 141° (b) Ls 165° (c)Ls 238°, with the CDOD plots appearing on the right.

Figure 11 displays synthetic satellite images of local Mars dust events during the year 14 Gebhardt et al. (2020) model simulation as a function of longitude and latitude. The color variation in the images demonstrates different atmospheric conditions; the brighter areas indicate locations with higher dust concentrations, while the darker is the opposite. Generally, Mars's atmosphere is quite hazy because it contains a considerable

amount of aerosols and suspended background dust. Under those circumstances, the observations and images of the Martian surface and atmosphere are disturbed by the scattering and absorption of solar light within aerosols (Christensen, 1988). The surface albedo was included as input in the model, as clear from Figure 11 in the changes of the surface CO2 ice. Hence, its effect appears on the degree of brightness of the synthetic satellite images, which makes it difficult to determine the location and extent of the storm. In that case, the interpretation of the satellite images of Mars should take into account the effects of the surface reflectance. For a clear estimation of the dust storm in the images, the MarsWRF CDOD plots are provided.

Different local dust storms are present in Figure 11 during the high dust loading season with commonly clear conditions over most of the planet, with small-scale dust activity occurring in the Hellas basin near the edge of the south polar cap and east Elysium Mons. Based on the CDOD, these small storms were not observed until after Ls 20° as the season progressed, and multiple local storms have been activated and formed frequently until the end of the MY. Figure 11(a) shows a local dust storm during the early high dust loading season on sol 302 Ls 141° lasts for only 3 sols. It takes almost the same extension and shape shown in the CDOD plot. During sol 347 (b), there are 2 local dust storms with an opacity of around 3 in the low-elevation regions of the southern hemisphere, both close to 50°S, one at Hellas (to the right) and the other at Argyre (to the left) lasting for a short duration (one sol only). Another image (c) of a local storm in the northern hemisphere near the east region of Elysium Mons on sol 468 at Ls 238°. This storm is difficult to detect in the synthetic satellite image because it rises in the bright albedo feature, as seen in Figure 6 in section 1.4, and because of the suspended background dust in the atmosphere. In general, the lifted dust does not travel long distances in these storms and mostly sediment back in the same area (Montabone & Forget, 2018).

3.2.2 Regional Dust Storms
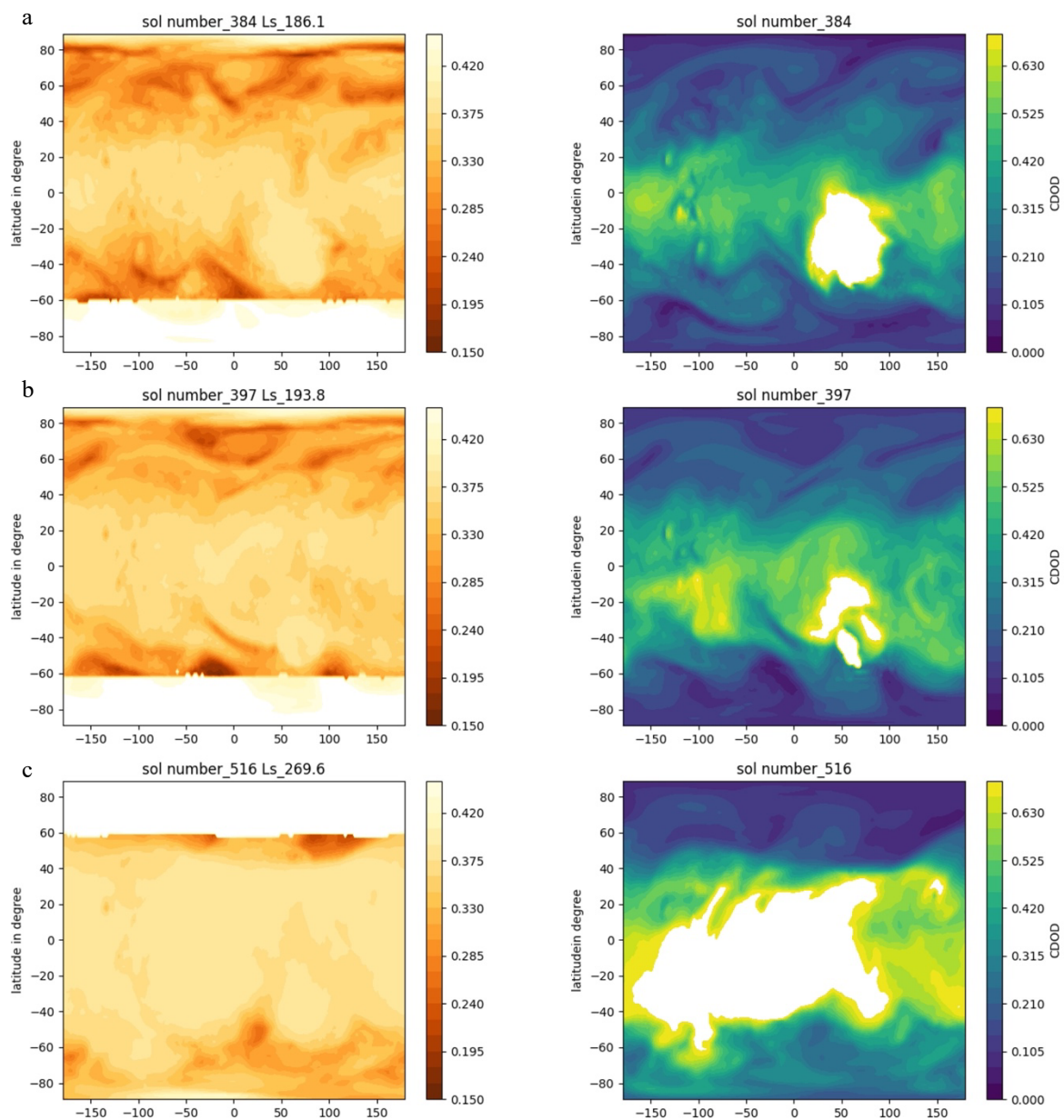
Figure 12: Synthetic satellite images (670 nm) in 2° × 2° grid resolution showing 3 separated regional dust storms. In MY14 of Gebhardt et al.(2020) model years at (a) sol 384 Ls 186° (b) sol 397 Ls 193° (c) sol 516 Ls 270°, with the CDOD plots on the right.

Lifted dust in a regional storm can travel long distances and can sediment in areas far from the origin (Montabone & Forget, 2018); this can be seen through images in Figure 12, where these events have a rapid migration toward the equatorial regions. Some regional dust storms can grow to affect about a third of the planet and endure up to a few weeks, while a few others can disturb half of the planet, covering the southern

hemisphere. A regional dust storm with 10 sols duration rose in the Hellas region in sol 381 (not shown) and spread in a broader range reaching its maximum in (a) sol 384 at Ls 186° and ending on sol 390 (not shown). The synthetic image appears brighter (higher concentration of dust) in the Hellas and equatorial zone as the opacity in these regions is almost 5 (not shown) and 1.5, respectively. The Hellas Basin is the main surface dust-lifting region during this storm; the dust cloud started in the south of the basin and reached the north by the end of the storm duration. The intensity of the regional storm (b) in sol 397 appears clearly in the CDOD plot, while in the synthetic image, it seems blurred and overlapped with atmospheric dust lifted in the equatorial region.

After this storm and for a period of 100 sols until sol 500 from Ls 193° to Ls 259°, no storms were observed except a few short and small local storms (number of 5 storms) in high latitude in the northern hemisphere. This gap between the dust activities is consistent with the solsticial pause phenomenon, which according to Montabone and Forget (2018), is one of the crucial features that can be seen in all MYs. Mainly, it is the decrease of the intensity of the baroclinic transient waves between Ls 230° and Ls 300°. Decreasing the intensity of surface winds will lead to a global decrease in dust loading with time between Ls 235° and Ls 264°. The dust settles and sediments back to the surface until it forms again and grows back as regional dust storms at Ls 270° in Figure 12(c), an intense regional dust storm in the early stage before the occurrence of the global dust storm. From the image, the storm appears to cover most of the latitude, but it initiated and expanded at equatorial latitudes south of Chryse Planitia, as clear in the CDOD plot. After sol 516 (not shown in the figure), the storm raised and developed further to obscure the southern hemisphere with more than 4.5 opacities at the most latitude and > 5.8 opacities in the storm's center, south of Chryse Planitia.

3.2.3 Expansion From Regional to Global
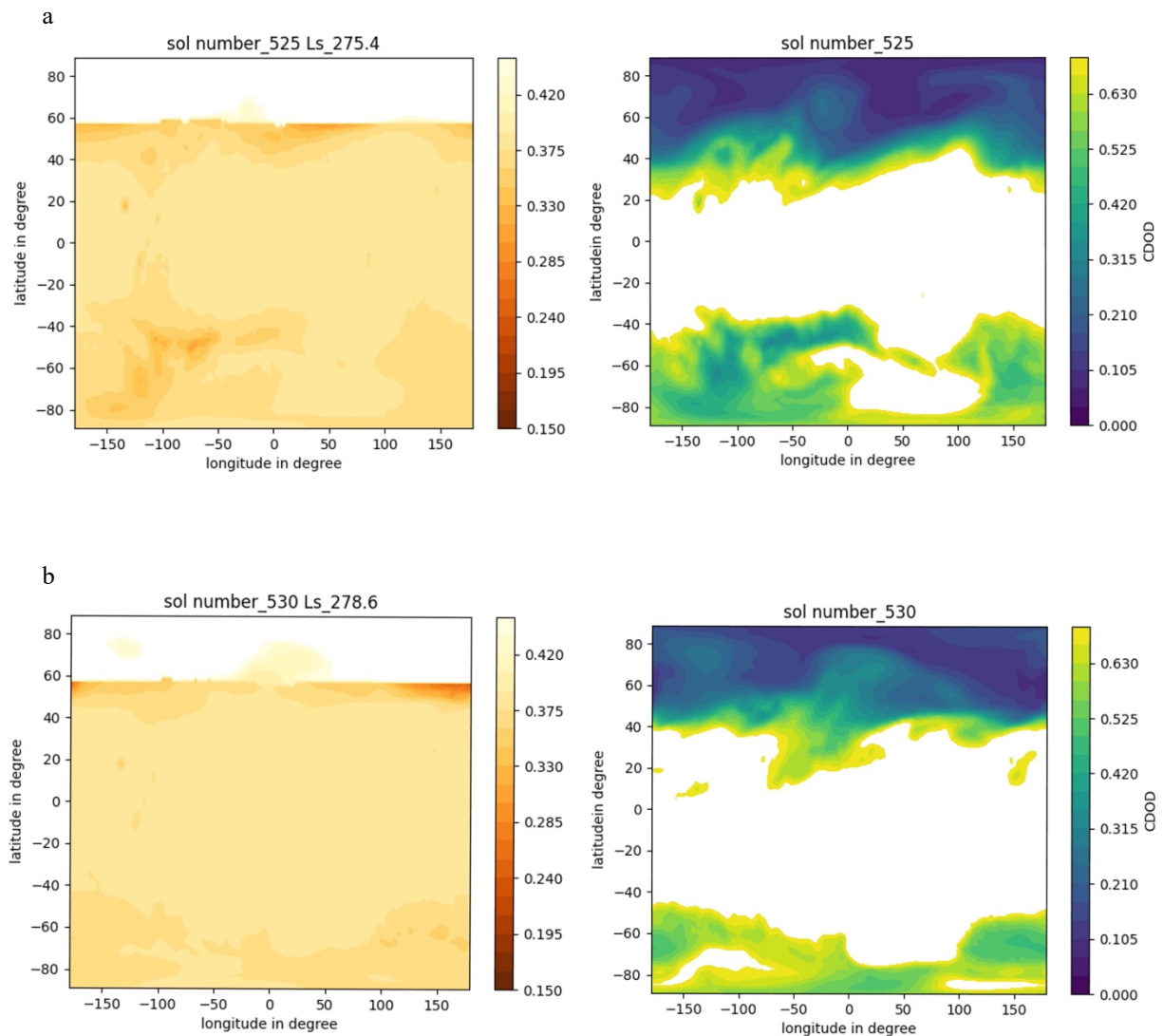
Figure 13: Synthetic satellite images (670 nm) in 2° × 2° grid resolution showing the expansion of regional dust storm to a global scale event. At (a) sol 525 Ls 275° (b) sol 530 Ls 278°, the CDOD plots appear on the right side of the figure.

From the synthetic satellite images in Figure 13, it is not straightforward to observe the surface change and dust movement during the development of the regional storm into a global one. The images show a complete obscuration of the surface by the dust, where the atmosphere was full of dust except for the surface ice of the north pole. The expansion started with 2 dust-lifting centers in the southern hemisphere. The growth

of two dust centers, especially in Hellas (b), led to their merger, causing the dusty conditions to extend and expand further.

3.2.4 Global Dust Events
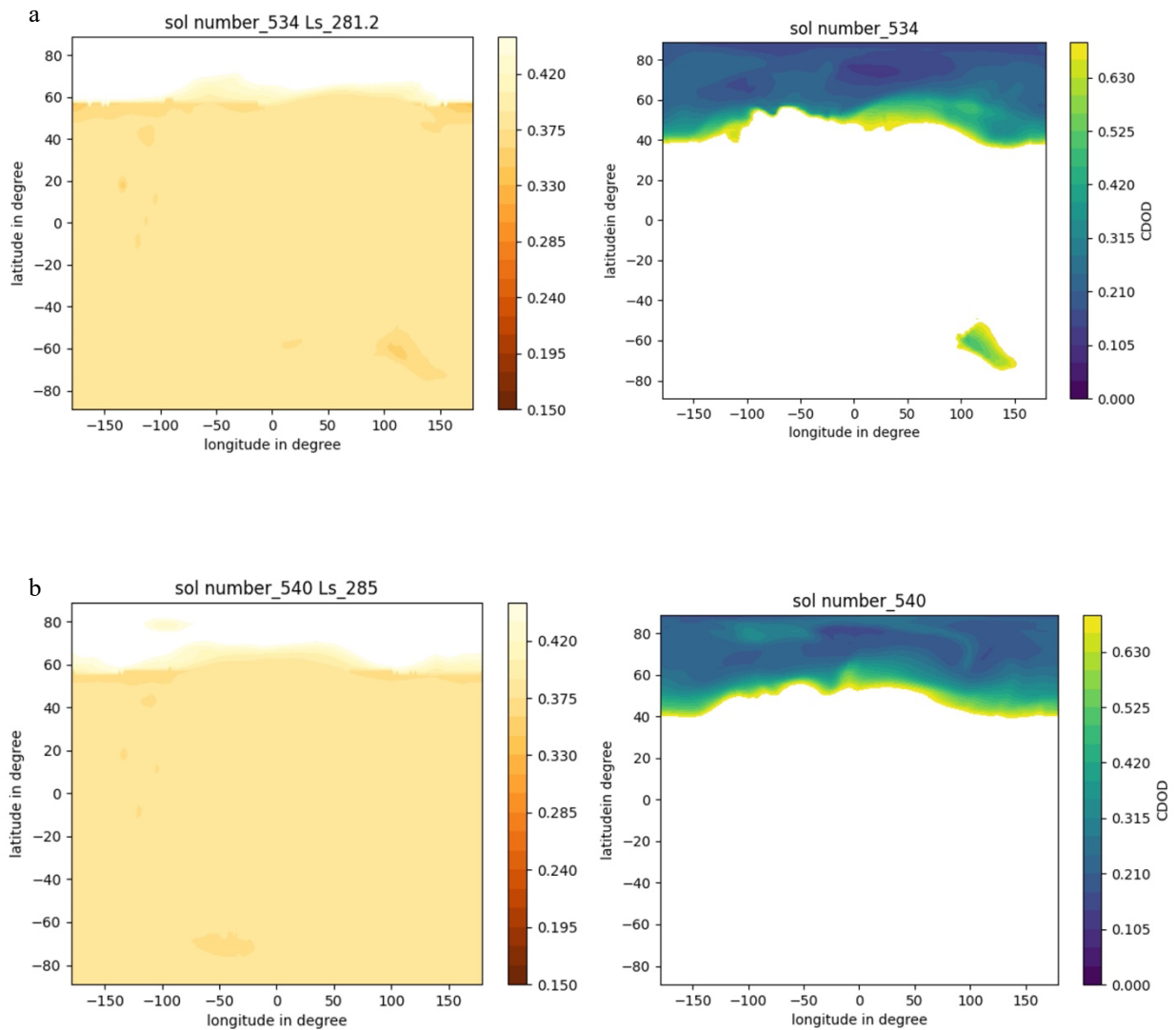
Figure 14: Synthetic satellite images (670 nm) in 2° × 2° grid resolution showing the effect of the Global dust storm event on the planet. In MY14 of Gebhardt et al.(2020) model years at (a) sol 534 Ls 281° (b) sol 540 Ls 285°, with the CDOD plots appearing on the right.

Montabone and Forget (2018) identified a global dust storm as the combination of multiple regional dust storms that actively lift dust particles over several, possibly connected areas (lifting centers). The expansion and merger between the main 2 dust-

lifting centers and minor surface dust lifting north of Olympus Mons were the main reason for the generation of the global dust storm, the largest spatial-scale dust-lifting event on Mars. Soon after the combination, a significant and sudden increase of predicted atmospheric dust occurred in the Hellas Planitia and south of Chryse Planitia regions, causing a dramatic change in the planet's appearance with the lifted dust globally distributed and dust clouds and haze raised and covered the whole planet. The storm grows larger above these regions, with opacities locally reaching roughly 6, according to values of the CDOD variable (not shown). That means the whole surface is blocked, and as known, under those circumstances, a small amount of solar light and radiation reaches the Martian surface.

Figure 14 presents images of the global dust storm in the MY 14 of the Gebhardt et al. (2020) model simulation run during the active dust season (the high dust loading season). These images give a clear and general perception of the planet's state during a global dust storm. Except for the northern polar latitude, the whole planet has one uniform brightness. The duration from Ls 278° to Ls 294° sol 530 to sol 555 considers the most intense period of dust accumulation throughout the whole MY. The phase of the storm in (a) sol 534 at Ls 281° and (b) sol 540 at Ls 285° is where this event reaches its peak and maximum, dust spread over large connected portions of the planet and lasting for weeks to months. Certainly, this is responsible for the reddish, dusty haze and other dust clouds seen across the planet in a latitudinal band, as shown in the satellite image in Figure 15. This phenomenon is responsible for the abrupt increase in temperature, as simulated in the T15 in Figure 9, where it has significant effects on diurnal pressure variations, atmospheric heating, and global circulation.

The dust continued to inject and lift to cover the atmosphere obscuring the planet until sol 600 Ls 322° when the amount of dust globally decreased with the highest value of CDOD measured close to 1. Typically, the decay phase of this type of event towards typical background dust levels can last for more than a hundred sols. In this case, the event lasted for more than 80 Martian sols. Even though the model is able to produce successful global storms, the too-slow decay of global dust storm events is a known shortcoming of the MarsWRF model. By the end of the Martian year, most dust has settled and sedimented back to the surface, only the background dust left suspended in

the atmosphere. Throughout the storm phase, it was observed that the atmosphere in the southern hemisphere had a greater amount of dust content compared to the northern hemisphere. During the decay phases, the southern hemisphere also retained dust for a longer duration than the northern hemisphere. After all, it is clear that this year of the MarsWRF model seems to feature various types of dust behavior at different times of the year at selected locations, particularly at southern mid- and high-latitudes.
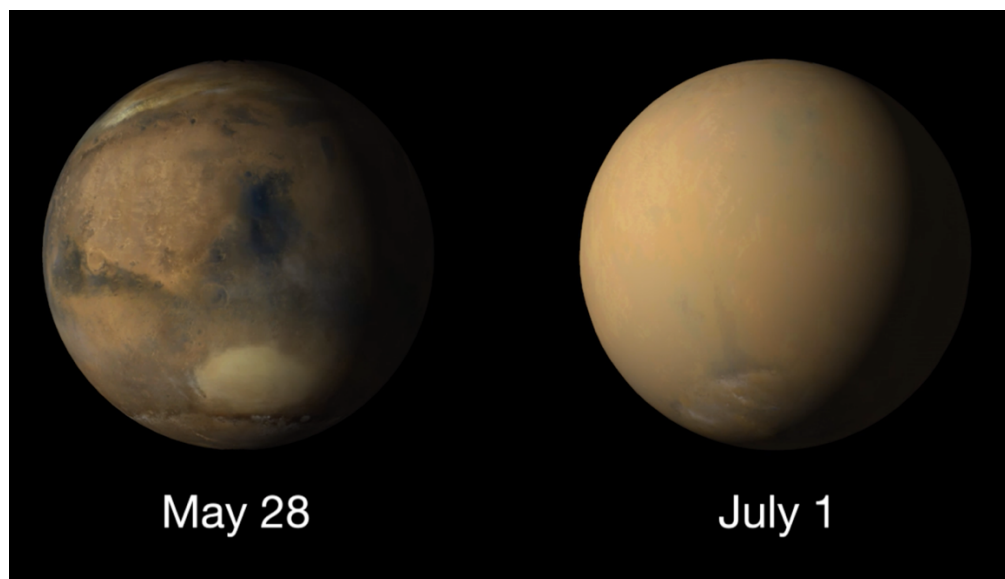

Figure 15: Shows a real satellite image during the 2018 global dust storm event in MY 34 at Ls 182.9° May 28 and Ls 202.8° July 1.

The image was taken by Mars Color Imager (MARCI) camera onboard Mars Reconnaissance Orbiter (MRO). This dust event caused a loss of contact between the Opportunity Rover and the Earth. (Mars.NASA.gov, n.d.)

During the clear atmospheric conditions, it is easy to recognize some features that appear on the planet, such as Valles Marineris (left), Meridiani center, an autumn dust storm in Acidalia (top), and the early spring south polar cap (bottom). The other image of the planet is from the same perspective, but the features are unidentifiable as most of the surface was overshadowed by the planet-encircling dust haze. The real satellite images are in line with the generated synthetic satellite images in this project, where the differences between the two images in Figure 15 are reflected in the differences between the produced TOA reflectance images under low-dust and high-dust conditions. The actual satellite and the synthetic images have the same presentation of a global dust

storm event and the same distribution of the tonal range. During these circumstances, the planet is entirely enveloped with dust blocking the view of the surface.

3.3 Synthetic Satellite Images with Zero Dust
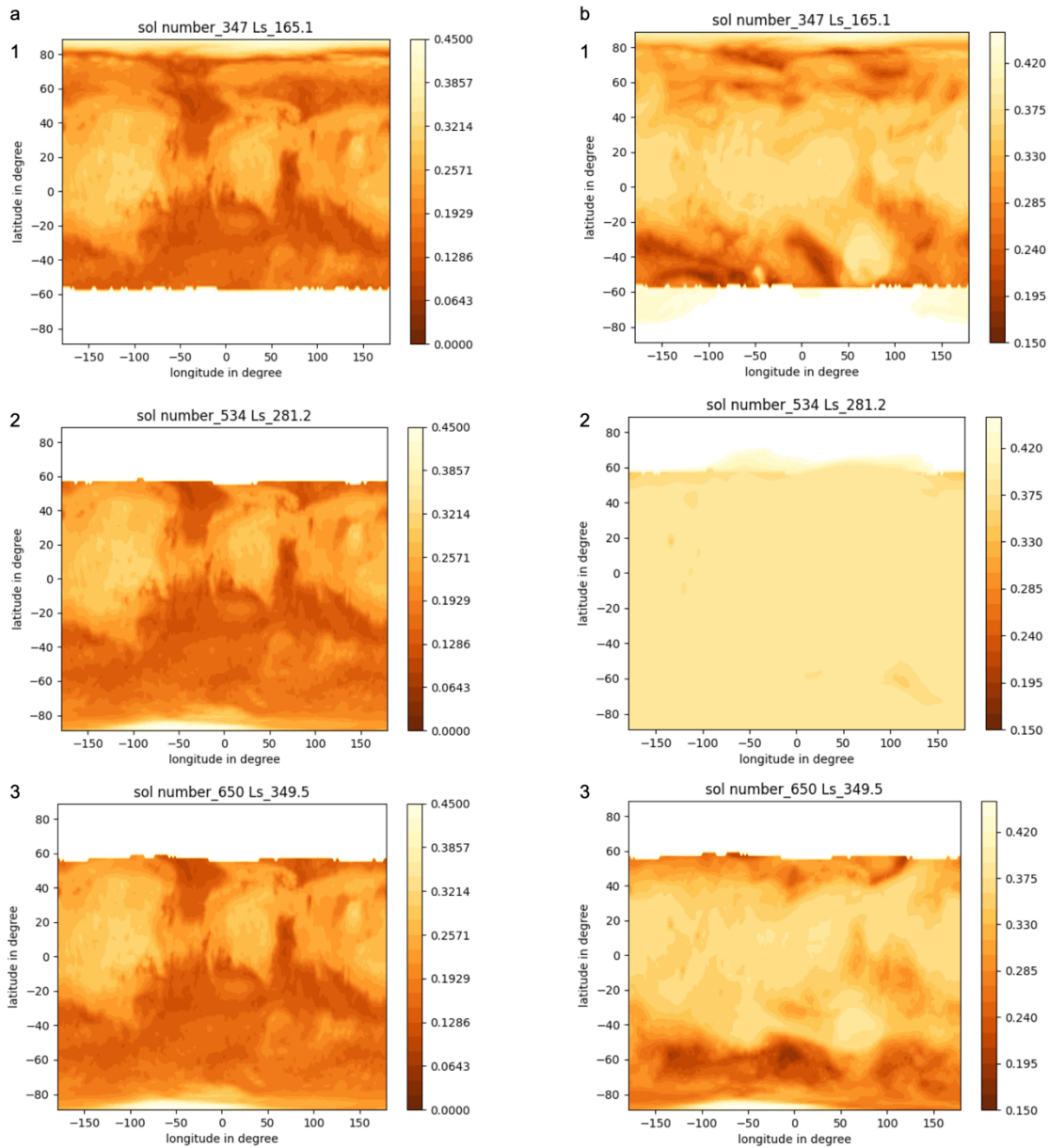
Figure 16: Synthetic satellite images 2° × 2° (670 nm) MY14 presenting (a) images without atmospheric dust (b) images with atmospheric dust. (1) local dust storm sol 347 Ls165° (2) global dust storm sol 534 Ls 281° (3) non-dusty condition sol 650 Ls ~350°

This project mainly focuses on Martian dust and the resulting synthetic satellite images aimed to capture the planet's condition during the different dust storms. The result images tend to appear saturated as the surface is brighter than expected due to the

surface albedo effect. Differences can be notable between the synthetic images and CDOD plots when comparing the same sols regarding the extent and spread of dust. As previously pointed out, the existence of the albedo is a source of uncertainty. It affects the contrast of the images, making the surface as bright as a dust. For this, isolating and removing the atmospheric dust as input and generating images with zero dust will clearly, identify how far albedo impacts the images, hence, verifying that the model produces reasonable results. A clear gradient of colors can be appreciated in Figure 16, which compares the two cases: (a) images without atmospheric dust and (b) regular images with atmospheric dust.

The model mainly consists of major arrays responsible for building the results; 1) the Rayleigh arrays, 2) the Dust arrays, and 3) surface reflection. Excluding the dust information means the images to the left represent the top of atmosphere reflectance of the Rayleigh scattering and surface reflectance. Images to the left are pretty similar to the albedo map Figure 6 in Section (1.4.8), and notably, all three images in (a) have the same pattern of the spatial distribution of the values, regardless of the changes in the surface CO_2 ice, especially a (2,3) both are identical. The reason is that the surface reflection is the same throughout the whole MY, unlike the dust distribution.

From Figure 16, it is clear how the shape of the albedo feature affects the brightness of the synthetic satellite images with dust events. Although the dust activity in b (1) took limited places in Hellas and Argyre, the image seems brighter in the equatorial region from 40 N to 40 S, roughly the same extent as the surface reflectance feature. The b (2) was the maximum phase of the global dust storm event, and the atmosphere was already covered completely with dust, so the albedo effect appears only as a high reflection of the northern pole. While the image of clear condition atmosphere b (c) clearly shows the impact of the surface albedo since no dust is lifted in the CDOD image (not shown), and the maximum opacity is around 0.5. Still, the synthetic image appears brighter than expected, as if it refers to the existence of dust activity.

Chapter 4: Conclusion

Atmospheric dust is a key element in understanding the climate system in general and dust storms in particular. In order to enhance our understanding of its environmental processes, we can take advantage of the accumulated data and the improved numerical models. This thesis provides an approach that can be employed to get images that simulate the behavior of atmospheric dust during a dust event on Mars. A radiative transfer model (DISORT) was applied to produce synthetic satellite images using output data from the (Gebhardt et al., 2020) MarsWRF model. These products contribute to adding value to the output data of the numerical models by using them in evaluating and refining the model performance. After the validation of the output data, they can be used to develop & verify satellite instruments.

Synthetic imagery can be used in the process of prediction and forecasting when it comes to future conditions and missions. Generally, the results of this work demonstrate this method can be successfully applied to Mars to get images of the Martian atmosphere that illustrate what the planet looks like during a dust storm event. Images have yielded important results regarding the dynamical process of development of the storms, starting from the beginning phase (dust lifting centers), the expansion of the dust storm, the regions it covers, and the atmospheric response for the dust loading. From the images, the region of Hellas can consider the primary lifting center as it is an obvious bright clear spot in all synthetic satellite images. However, the other 3 enhanced dust lifting centers appear at the beginning of any storm event during this MY; they can be detected easily from opacity distribution plots.

These results, however, must be interpreted with taking into account some of the limitations. To illustrate, high contrast of images is essential and needed to get a clear view of the dust distribution, but the degree of contrast in the images was low because of the confusion between inputs of dust and albedo, which makes it challenging to analyze the images and hard to distinguish the surface reflections from the dust accumulations. That's why synthetic images were shown in conjunction with the opacity plots (column dust optical depth). To highlight the critical effect and the overlap between the two inputs, images with dust and images with no dust input are presented, which gives an

idea about how far the albedo disturbs the detection of dust on the planet's surface (dust lifting centers extent and receding). Another limitation was with the model MarsWRF; the synthetic images presented in this work were plotted on the MY14 of the MarsWRF model run of (Gebhardt et al., 2020). The Martian years are just simulated years of the model itself; they didn't simulate or represent a specific year or day of Mars. Mainly, one of the thesis's aims is to compare the top-of-atmosphere radiances with real data, and that can't be done directly with the simulated year of the model. To overcome the comparison constraints, Mars PCM can be a better and more realistic model, providing real dust observations and reproducing specific years. Mars PCM is a Global Climate Model and was used several times as a validation tool by comparing it with other established Mars models. So the generated synthetic satellite images in this work can be directly compared with the real satellite images if Mars PCM was used.

Hopefully, this method can contribute to the study and knowledge of Mars in general and support the exploration of new, more unanswered questions about these dust flows in the Martian environment in at least a few ways. Furthermore, in this work, an attempt to optimize the quality of the generated synthetic images was done by validating them by comparing the synthetic imagery with the real images taken from satellites orbiting Mars and trying to estimate their similarities. The optimizing process can be done more broadly by experimenting with different data visualization settings, for example, improving the quality of input data, using higher-resolution input data and processing techniques, which will enhance the visual quality of the images and get more detailed and accurate results. Also, machine learning algorithms can be used to improve the accuracy and resolution of synthetic satellite images by learning from high-quality reference data and applying this knowledge to generate higher-quality synthetic images.

In the course of this process, one of the scientific objectives of the EMM was set to focus on a better understanding of the lower atmosphere, which was achieved by using measurements from different instruments, including the Emirates eXploration Imager. The EXI instrument is a multi-wavelength radiation-tolerant camera that provides images of the Martian atmosphere. Its covers the wavelength band UV-A (305 – 335 nm), Red (625 – 645 nm), Green (506 - 586 nm), and Blue (405 – 469 nm) (Almatroushi et al., 2021). This mission successfully tracks different dust events ranging from local to

regional and large regional dust storms. We can take advantage of the revealed EXI observation and data to get images of recent dust storm events in selected wavelength bands, then match them with the synthetic satellite images plotted in the same conditions and wavelengths. This process can help analyze both the real and synthetic satellite images and derive characteristics of the atmospheric dust coverage and storm features in general.

References

Almatroushi, H., AlMazmi, H., AlMheiri, N., AlShamsi, M., AlTunaiji, E., Badri, K., Lillis, R. J., Lootah, F., Yousuf, M., Amiri, S., Brain, D. A., Chaffin, M., Deighan, J., Edwards, C. S., Forget, F., Smith, M. D., Wolff, M. J., Christensen, P. R., England, S., … Young, R. M. B. (2021). Emirates Mars Mission Characterization of Mars Atmosphere Dynamics and Processes. *Space Science Reviews*, *217*(8), 89. https://doi.org/10.1007/s11214-021-00851-6

Amiri, H. E. S., Brain, D., Sharaf, O., Withnell, P., McGrath, M., Alloghani, M., Al Awadhi, M., Al Dhafri, S., Al Hamadi, O., Al Matroushi, H., Al Shamsi, Z., Al Shehhi, O., Chaffin, M., Deighan, J., Edwards, C., Ferrington, N., Harter, B., Holsclaw, G., Kelly, M., … Yousuf, M. (2022). The Emirates Mars Mission. *Space Science Reviews*, *218*(1), 4. https://doi.org/10.1007/s11214-021-00868-x

Basu, S. (2004). Simulation of the Martian dust cycle with the GFDL Mars GCM. *Journal of Geophysical Research*, *109*(E11), E11006. https://doi.org/10.1029/2004JE002243

Battalio, M., & Wang, H. (2019). The Aonia-Solis-Valles dust storm track in the southern hemisphere of Mars. *Icarus*, *321*, 367–378. https://doi.org/10.1016/j.icarus.2018.10.026

Battalio, M., & Wang, H. (2021). The Mars Dust Activity Database (MDAD): A comprehensive statistical study of dust storm sequences. *Icarus*, *354*, 114059. https://doi.org/10.1016/j.icarus.2020.114059

Bertrand, T., Wilson, R. J., Kahre, M. A., Urata, R., & Kling, A. (2020). Simulation of the 2018 Global Dust Storm on Mars Using the NASA Ames Mars GCM: A Multitracer Approach. *Journal of Geophysical Research: Planets*, *125*(7). https://doi.org/10.1029/2019JE006122

Bikos, D., Lindsey, D. T., Otkin, J., Sieglaff, J., Grasso, L., Siewert, C., Correia, J., Coniglio, M., Rabin, R., Kain, J. S., & Dembek, S. (2012). Synthetic Satellite Imagery for Real-Time High-Resolution Model Evaluation. *Weather and Forecasting*, *27*(3), 784–795. https://doi.org/10.1175/WAF-D-11-00130.1

Byrne, S., Zuber, M. T., & Neumann, G. A. (2008). Interannual and seasonal behavior of Martian residual ice-cap albedo. *Planetary and Space Science*, *56*(2), 194–211. https://doi.org/10.1016/j.pss.2006.03.018

Cantor, B. A. (2007). MOC observations of the 2001 Mars planet-encircling dust storm. *Icarus*, *186*(1), 60–96. https://doi.org/10.1016/j.icarus.2006.08.019

Cantor, B. A., James, P. B., Caplinger, M., & Wolff, M. J. (2001). Martian dust storms: 1999 Mars Orbiter Camera observations. *Journal of Geophysical Research: Planets*, *106*(E10), 23653–23687. https://doi.org/10.1029/2000JE001310

Cantor, B. A., Kanak, K. M., & Edgett, K. S. (2006). Mars Orbiter Camera observations of Martian dust devils and their tracks (September 1997 to January 2006) and evaluation of theoretical vortex models. *Journal of Geophysical Research: Planets*, *111*(E12), n/a-n/a. https://doi.org/10.1029/2006JE002700

Cantor, B. A., Pickett, N. B., Malin, M. C., Lee, S. W., Wolff, M. J., & Caplinger, M. A. (2019). Martian dust storm activity near the Mars 2020 candidate landing sites: MRO-MARCI observations from Mars years 28–34. *Icarus*, *321*, 161–170. https://doi.org/10.1016/j.icarus.2018.10.005

Chen-Chen, H., Pérez-Hoyos, S., & Sánchez-Lavega, A. (2021). Dust particle size, shape and optical depth during the 2018/MY34 martian global dust storm retrieved by MSL Curiosity rover Navigation Cameras. *Icarus*, *354*, 114021. https://doi.org/10.1016/j.icarus.2020.114021

Chow, K.-C., Chan, K., & Xiao, J. (2018). Dust activity over the Hellas basin of Mars during the period of southern spring equinox. *Icarus*, *311*, 306–316. https://doi.org/10.1016/j.icarus.2018.04.011

Christensen, P. R. (1988). Global albedo variations on Mars: Implications for active aeolian transport, deposition, and erosion. *Journal of Geophysical Research*, *93*(B7), 7611. https://doi.org/10.1029/JB093iB07p07611

Clancy, R. T., Wolff, M. J., Whitney, B. A., Cantor, B. A., Smith, M. D., & McConnochie, T. H. (2010). Extension of atmospheric dust loading to high altitudes during the 2001 Mars dust storm: MGS TES limb observations. *Icarus*, *207*(1), 98–109. https://doi.org/10.1016/j.icarus.2009.10.011

Clough, S. A., Shephard, M. W., Mlawer, E. J., Delamere, J. S., Iacono, M. J., Cady-Pereira, K., Boukabara, S., & Brown, P. D. (2005). Atmospheric radiative transfer modeling: a summary of the AER codes. *Journal of Quantitative Spectroscopy and Radiative Transfer*, *91*(2), 233–244. https://doi.org/10.1016/j.jqsrt.2004.05.058

Fedorova, A. A., Montmessin, F., Rodin, A. V., Korablev, O. I., Määttänen, A., Maltagliati, L., & Bertaux, J.-L. (2014). Evidence for a bimodal size distribution for the suspended aerosol particles on Mars. *Icarus*, *231*, 239–260. https://doi.org/10.1016/j.icarus.2013.12.015

Fenton, L. K., Geissler, P. E., & Haberle, R. M. (2007). Global warming and climate forcing by recent albedo changes on Mars. *Nature*, *446*(7136), 646–649. https://doi.org/10.1038/nature05718

Forget, F., & Montabone, L. (2017, July 16). Atmospheric Dust on Mars: A Review. *47th International Conference on Environmental Systems*.

Gebhardt, C., Abuelgasim, A., Fonseca, R. M., Martín-Torres, J., & Zorzano, M. -P. (2020). Fully Interactive and Refined Resolution Simulations of the Martian Dust Cycle by the MarsWRF Model. *Journal of Geophysical Research: Planets*, *125*(9). https://doi.org/10.1029/2019JE006253

Gebhardt, C., Abuelgasim, A., Fonseca, R. M., Martín-Torres, J., & Zorzano, M. -P. (2021). Characterizing Dust-Radiation Feedback and Refining the Horizontal Resolution of the MarsWRF Model Down to 0.5 Degree. *Journal of Geophysical Research: Planets*, *126*(3). https://doi.org/10.1029/2020JE006672

Grasso, L. D., Sengupta, M., Dostalek, J. F., Brummer, R., & Demaria, M. (2008). Synthetic satellite imagery for current and future environmental satellites. *International Journal of Remote Sensing*, *29*(15), 4373–4384. https://doi.org/10.1080/01431160801891820

Guzewich, S. D., Lemmon, M., Smith, C. L., Martinez, G., de Vicente-Retortillo, A., Newman, C. E., et al. (2019). Mars science laboratory observations of the 2018/Mars year 34 global dust storm. *Geophysical Research Letters*, *46*, 71–79. https://doi.org/10.1029/2018GL080839

Heavens, N. G., Cantor, B. A., Hayne, P. O., Kass, D. M., Kleinböhl, A., McCleese, D. J., Piqueux, S., Schofield, J. T., & Shirley, J. H. (2015). Extreme detached dust layers near Martian volcanoes: Evidence for dust transport by mesoscale circulations forced by high topography. *Geophysical Research Letters*, *42*(10), 3730–3738. https://doi.org/10.1002/2015GL064004

Haberle, R. M. (2003). PLANETARY ATMOSPHERES | Mars. In *Encyclopedia of Atmospheric Sciences* (pp. 1745–1755). Elsevier. https://doi.org/10.1016/B0-12-227090-8/00312-2

Haberle, R. M., Clancy, R. T., Forget, F., & Smith, M. D. (2017). *The Atmosphere and Climate of Mars*. Cambridge University Press.

Hueso, R., Newman, C. E., del Río-Gaztelurrutia, T., Munguira, A., Sánchez-Lavega, A., Toledo, D., Apéstigue, V., Arruego, I., Vicente-Retortillo, A., Martínez, G., Lemmon, M., Lorenz, R., Richardson, M., Viudez-Moreiras, D., de la Torre-Juarez, M., Rodríguez-Manfredi, J. A., Tamppari, L. K., Murdoch, N., Navarro-López, S., … Lepinette-Malvite, A. (2023). Convective Vortices and Dust Devils Detected and Characterized by Mars 2020. *Journal of Geophysical Research: Planets*, *128*(2). https://doi.org/10.1029/2022JE007516

Kahanpää, H., Newman, C., Moores, J., Zorzano, M. -P., Martín-Torres, J., Navarro, S., Lepinette, A., Cantor, B., Lemmon, M. T., Valentín-Serrano, P., Ullán, A., & Schmidt, W. (2016). Convective vortices and dust devils at the MSL landing site: Annual variability. *Journal of Geophysical Research: Planets*, *121*(8), 1514–1549. https://doi.org/10.1002/2016JE005027

Kass, D. M., Kleinböhl, A., McCleese, D. J., Schofield, J. T., & Smith, M. D. (2016). Interannual similarity in the Martian atmosphere during the dust storm season. *Geophysical Research Letters*, *43*(12), 6111–6118. https://doi.org/10.1002/2016GL068978

Kconnour.github. Retrieved March 1, 2023, from https://kconnour.github.io/pyRT_DISORT/rst/about-this-project/about-pyRT_DISORT.html

Kelly, N. J., Boynton, W. v., Kerry, K., Hamara, D., Janes, D., Reedy, R. C., Kim, K. J., & Haberle, R. M. (2007). Seasonal polar carbon dioxide frost on Mars: CO_2 mass and columnar thickness distribution. *Journal of Geophysical Research*, *112*(E3), E03S07. https://doi.org/10.1029/2006JE002678

Lin, Z., Stamnes, S., Jin, Z., Laszlo, I., Tsay, S.-C., Wiscombe, W. J., & Stamnes, K. (2015). Improved discrete ordinate solutions in the presence of an anisotropically reflecting lower boundary: Upgrades of the DISORT computational tool. *Journal of Quantitative Spectroscopy and Radiative Transfer*, *157*, 119–134. https://doi.org/10.1016/j.jqsrt.2015.02.014

Mars.NASA.gov. *Mars Before and After Dust Storm*. NASA Mars Exploration. Retrieved March 1, 2023, from https://mars.nasa.gov/resources/21961/mars-before-and-after-dust-storm

Montabone, L., & Forget, F. (2018, July 8). On Forecasting Dust Storms on Mars. *48th International Conference on Environmental Systems*.

Montabone, L., Forget, F., Millour, E., Wilson, R. J., Lewis, S. R., Cantor, B., Kass, D., Kleinböhl, A., Lemmon, M. T., Smith, M. D., & Wolff, M. J. (2015). Eight-year climatology of dust optical depth on Mars. *Icarus*, *251*, 65–95. https://doi.org/10.1016/j.icarus.2014.12.034

Montabone, L., Lewis, S. R., & Read, P. L. (2005). Interannual variability of Martian dust storms in assimilation of several years of Mars global surveyor observations. *Advances in Space Research*, *36*(11), 2146–2155. https://doi.org/10.1016/j.asr.2005.07.047

Montabone, L., Spiga, A., Kass, D. M., Kleinböhl, A., Forget, F., & Millour, E. (2020). Martian Year 34 Column Dust Climatology from Mars Climate Sounder Observations: Reconstructed Maps and Model Simulations. *Journal of Geophysical Research: Planets*, *125*(8). https://doi.org/10.1029/2019JE006111

NASA Image Gallery. Retrieved May 17, 2023, from https://attic.gsfc.nasa.gov/mola/images.html

National Center for Atmospheric Research, Mesoscale and Microscale Meteorology Division. (2011). *ARW version 3 Modeling System User's Guide.* https://www.inscc.utah.edu/~u0140878/dps/lair/la/plot/ARWUsersGuideV3.4.pdf

Newman, C. E., Hueso, R., Lemmon, M. T., Munguira, A., Vicente-Retortillo, Á., Apestigue, V., Martínez, G. M., Toledo, D., Sullivan, R., Herkenhoff, K. E., de la Torre Juárez, M., Richardson, M. I., Stott, A. E., Murdoch, N., Sanchez-Lavega, A., Wolff, M. J., Arruego, I., Sebastián, E., Navarro, S., … Guzewich, S. D. (2022). The dynamic atmospheric and aeolian environment of Jezero crater, Mars. *Science Advances*, *8*(21). https://doi.org/10.1126/sciadv.abn3783

Newman, C. E., Lee, C., Mischna, M. A., Richardson, M. I., & Shirley, J. H. (2019). An initial assessment of the impact of postulated orbit-spin coupling on Mars dust storm variability in fully interactive dust simulations. *Icarus*, *317*, 649–668. https://doi.org/10.1016/j.icarus.2018.07.023

Newman, C. E., Lewis, S. R., Read, P. L., & Forget, F. (2002). Modeling the Martian dust cycle, 1. Representations of dust transport processes. *Journal of Geophysical Research: Planets*, *107*(E12), 6-1-6–18. https://doi.org/10.1029/2002JE001910

Newman, C. E., & Richardson, M. I. (2015). The impact of surface dust source exhaustion on the martian dust cycle, dust storms and interannual variability, as simulated by the MarsWRF General Circulation Model. *Icarus*, *257*, 47–87. https://doi.org/10.1016/j.icarus.2015.03.030

Ordonez-Etxeberria, I., Hueso, R., Sánchez-Lavega, A., & Vicente-Retortillo, Á. (2020). Characterization of a local dust storm on Mars with REMS/MSL measurements and MARCI/MRO images. *Icarus*, *338*, 113521. https://doi.org/10.1016/j.icarus.2019.113521

Petrova, E. V., Hoekzema, N. M., Markiewicz, W. J., Thomas, N., & Stenzel, O. J. (2012). Optical depth of the Martian atmosphere and surface albedo from high-resolution orbiter images. *Planetary and Space Science*, *60*(1), 287–296. https://doi.org/10.1016/j.pss.2011.09.008

PSA UI. Retrieved May 17, 2023, from https://archives.esac.esa.int/psa/#!Table%20View/VMC%20(Mars%20Express)=instrument

Rafkin, S. C. R. (2009). A positive radiative-dynamic feedback mechanism for the maintenance and growth of Martian dust storms. *Journal of Geophysical Research*, *114*(E1), E01009. https://doi.org/10.1029/2008JE003217

Richardson, M. I. (2002). Investigation of the nature and stability of the Martian seasonal water cycle with a general circulation model. *Journal of Geophysical Research*, *107*(E5), 5031. https://doi.org/10.1029/2001JE001536

Richardson, M., Toigo, A., & Newman, C. (2007). Marswrf: A General Purpose, Local To Global Numerical Model For The Martian Climate And Atmosphere. A. *Seventh International Conference on Mars. 1353*, 3324.

Shirley, J. H., McKim, R. J., Battalio, J. M., & Kass, D. M. (2020). Orbit-Spin Coupling and the Triggering of the Martian Planet-Encircling Dust Storm of 2018. *Journal of Geophysical Research: Planets*, *125*(6). https://doi.org/10.1029/2019JE006077

Shirley, J. H., Newman, C. E., Mischna, M. A., & Richardson, M. I. (2019). Replication of the historic record of martian global dust storm occurrence in an atmospheric general circulation model. *Icarus*, *317*, 197–208. https://doi.org/10.1016/j.icarus.2018.07.024

Skamarock, W. C., Klemp, J. B., Dudhia, J., Gill, D. O., Barker, D. M., Wang, W., & Powers, J. G. (2008). *A Description of the Advanced Research WRF Version 2.*

Stamnes, K., Tsay, S.-Chee, Laszlo, Istvan, & Wiscombe, Warren. (2000). *DISORT, a General-Purpose Fortran Program for Discrete-Ordinate-Method Radiative Transfer in Scattering and Emitting Layered Media: Documentation of Methodology* (1.1; p. 107). NASA Goddard Space Flight Center

Stamnes, K., Tsay, S.-C., Wiscombe, W., & Jayaweera, K. (1988). Numerically stable algorithm for discrete-ordinate-method radiative transfer in multiple scattering and emitting layered media. *Applied Optics*, *27*(12), 2502. https://doi.org/10.1364/AO.27.002502

Strausberg, M. J. (2005). Observations of the initiation and evolution of the 2001 Mars global dust storm. *Journal of Geophysical Research*, *110*(E2), E02006. https://doi.org/10.1029/2004JE002361

Toigo, A. D., Lee, C., Newman, C. E., & Richardson, M. I. (2012). The impact of resolution on the dynamics of the martian global atmosphere: Varying resolution studies with the MarsWRF GCM. *Icarus*, *221*(1), 276–288. https://doi.org/10.1016/j.icarus.2012.07.020

Toigo, A. D., Richardson, M. I., John Wilson, R., & Wang, H. W. (2002). A first look at dust lifting and dust storms near the south pole of Mars with a mesoscale model. *Journal of Geophysical Research*, *107*(E7), 5050. https://doi.org/10.1029/2001JE001592

Toigo, A. D., Richardson, M. I., Wang, H., Guzewich, S. D., & Newman, C. E. (2018). The cascade from local to global dust storms on Mars: Temporal and spatial thresholds on thermal and dynamical feedback. *Icarus*, *302*, 514–536. https://doi.org/10.1016/j.icarus.2017.11.032

Vidot, J. (2014, September). Overview of the status of radiative transfer models for satellite data assimilation. In *Proceedings of the Seminar on Use of Satellite Observations in Numerical Weather Prediction*, *Reading, UK* (pp. 8-12).

Vincendon, M., Audouard, J., Altieri, F., & Ody, A. (2015). Mars Express measurements of surface albedo changes over 2004–2010. *Icarus*, *251*, 145–163. https://doi.org/10.1016/j.icarus.2014.10.029

Wang, H. (2003). Cyclones, tides, and the origin of a cross-equatorial dust storm on Mars. *Geophysical Research Letters*, *30*(9), 1488. https://doi.org/10.1029/2002GL016828

Wang, H., & Richardson, M. I. (2015). The origin, evolution, and trajectory of large dust storms on Mars during Mars years 24–30 (1999–2011). *Icarus*, *251*, 112–127. https://doi.org/10.1016/j.icarus.2013.10.033

Webster, G. (2016, June 9). *NASA Mars Orbiters Reveal Seasonal Dust Storm Pattern* [Text]. NASA. http://www.nasa.gov/feature/jpl/nasa-mars-orbiters-reveal-seasonal-dust-storm-pattern

Wells, E. N., Veverka, J., & Thomas, P. (1984). Mars: Experimental study of albedo changes caused by dust fallout. *Icarus*, *58*(3), 331–338. https://doi.org/10.1016/0019-1035(84)90079-4

Wolff, M. J., Smith, M. D., Clancy, R. T., Arvidson, R., Kahre, M., Seelos, F., Murchie, S., & Savijärvi, H. (2009). Wavelength dependence of dust aerosol single scattering albedo as observed by the Compact Reconnaissance Imaging Spectrometer. *Journal of Geophysical Research*, *114*, E00D04. https://doi.org/10.1029/2009JE003350

Wolff, M., Lopéz-Valverde, M., Madeleine, J., Wilson, R., Smith, M., Fouchet, T., & Delory, G. (2017). Radiative Process: Techniques and Applications. In R. Haberle, R. Clancy, F. Forget, M. Smith, & R. Zurek (Eds.), *The Atmosphere and Climate of Mars* (Cambridge Planetary Science, pp. 106-171). Cambridge: Cambridge University Press. doi:10.1017/9781139060172.006

Young, R. M. B., Millour, E., Guerlet, S., Forget, F., Ignatiev, N., Grigoriev, A. V., Shakun, A. V., Trokhimovskiy, A., Montmessin, F., & Korablev, O. (2022). Assimilation of Temperatures and Column Dust Opacities Measured by ExoMars TGO-ACS-TIRVIM During the MY34 Global Dust Storm. *Journal of Geophysical Research: Planets*, *127*(9). https://doi.org/10.1029/2022JE007312

Dust events on Mars range from local/regional dust storms that occur every MY to global dust storm storms that have only been observed, on average, once every 3-4 MYs. This project aims to convert MarsWRF output data into synthetic satellite images of Mars dust storms in different ranges by using the radiative transfer model DISORT. The main results are synthetic satellite images plotted in 670 nm with a grid resolution of $2° \times 2°$, they found to be consistent with the real cases of satellite images of Mars dust storms.

Fatima Alkaabi received her received her Master of Science in Space Science from the Department of Physics, College of Science and her Bachelor of Arts in Geography Track: Geoinformatics from the College of Humanities & Social Sciences, United Arab Emirates University, United Arab Emirates.

www.uaeu.ac.ae

عمادة المكتبات
Libraries Deanship

جامعة الإمارات العربية المتحدة
United Arab Emirates University

Digital Library Services Section - قسم الخدمات المكتبية الرقمية